Forward-time and backward-time isochrons, and their interactions

Peter Langfield, Bernd Krauskopf and Hinke M. Osinga
Department of Mathematics, The University of Auckland,
Private Bag 92019, Auckland 1142, New Zealand

February 2015

Abstract

We consider isochrons of a periodic orbit in the FitzHugh-Nagumo system, that is, the curves of points that converge to the periodic orbit in phase with each other, and we extend this notion to isochrons of a focus equilibrium. We introduce the notion of backward-time isochrons, which are isochrons of the reversed-time system, and show that a bifurcation occurs by way of a tangency between a set of forward-time and backward-time isochrons. We call this bifurcation a cubic isochron foliation tangency, or CIFT bifurcation. This bifurcation is not a local feature but happens globally throughout the annulus where both sets of isochrons coexist. We construct and discuss examples for three mechanisms for a CIFT bifurcation: a global time-scale separation; a perturbation that increases the velocity along trajectories in a local region of phase space; and a canard explosion (in the Van der Pol system).

1 Introduction

The response of oscillators to external stimulation provides a mechanism to understand its underlying dynamics. A mathematical model can be validated by ensuring that the responses from (external) perturbations away from a periodic orbit agree with the responses from external stimulations in the system being modeled. This technique has been applied in particular in the study of biological oscillators.

When applying the stimulation, small variations such as the intrinsic background noise, can significantly affect the measured response. Mathematically, this means that the basin of attraction, which is made up of all initial points that converge to the periodic orbit, exhibits regions of phase sensitivity. This is characterized by large changes in phase as a result of small variations in initial conditions. Even though each point in the basin approaches the periodic orbit, the trajectory may pass through faster or slower regions of phase space, and two points that are initially close together may have trajectories that approach the periodic orbit significantly out of phase with each other. It is important to know when such sensitivity arises in the system, and where the particular regions of sensitivity are. For example, Nabi *et al.* use knowledge of regions of phase sensitivity to desynchronize a network of oscillators [21]. Each oscillator in the network is perturbed to the region of phase sensitivity, such that the addition of noise is sufficient to desynchronize the oscillators.

The change in phase as a result of a given perturbation is closely related to the notion of an isochron. An isochron is the set of points with the same asymptotic phase, that is, the phase with which a point in the basin of attraction converges to the periodic orbit. Winfree defined isochrons and asymptotic phase in 1974 [28]; see also section Section 2. Subsequently, Guckenheimer [10] related isochrons to manifold theory [12]: he explained that for a periodic orbit Γ with period T_Γ, each isochron $I(\gamma)$ is the stable manifold of the time-T_Γ map associated with the fixed point γ on Γ. As a consequence, the set of all the isochrons forms a foliation of the basin of attraction.

We illustrate the notion of an isochron with an example model that is similar in style to a model by Winfree [29, pp.174]; see also Section 3. Figure 1(a) shows ten isochrons for this model. The isochrons are associated with the attracting periodic orbit Γ (black), and are uniformly distributed in phase. The point $\gamma_0 \in \Gamma$ is assigned zero phase and the other phases are defined accordingly; usually, γ_0 is chosen as the maximum point on Γ with respect to the x-variable. Each isochron has a unique color, which corresponds to its phase as shown

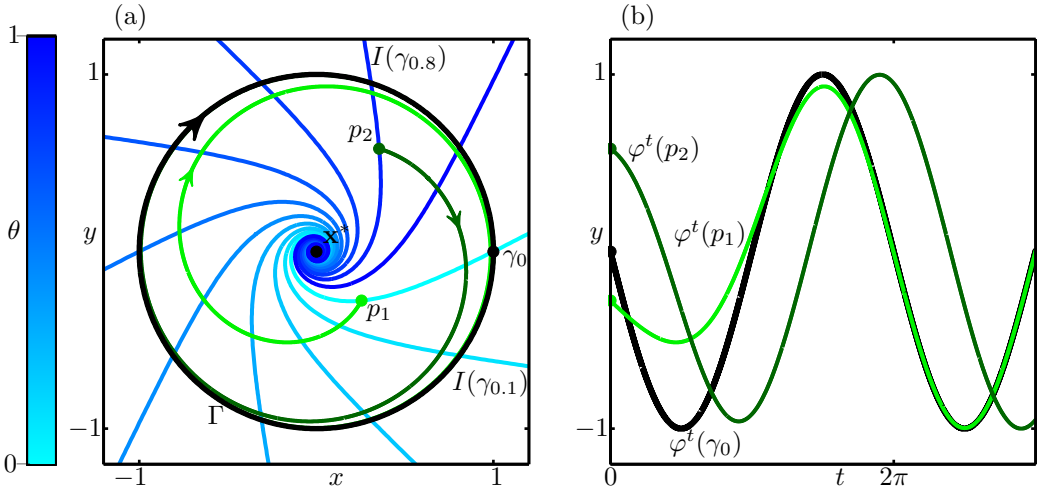

Figure 1: Panel (a) shows ten isochrons of the periodic orbit Γ; the isochrons are uniformly distributed in phase and colored according to their associated phases as indicated by the color bar relative to γ_0. Also shown are orbits $\phi^t(p_1)$ and $\phi^t(p_2)$ that start on two different isochrons at the points p_1 and p_2, respectively. Panel (b) shows the time series of the y-coordinates of $\phi^t(\gamma_0)$, $\phi^t(p_1)$ and $\phi^t(p_2)$.

by the color bar. The isochrons accumulate on a repelling equilibrium $\mathbf{x}^*$. Note that $\mathbf{x}^*$ lies on the boundary of the basin of attraction of Γ, which is called the phaseless set of Γ. Also shown are the trajectories $\varphi^t(p_1)$ and $\varphi^t(p_2)$ of two points p_1 and p_2. Since $\gamma_0 \in \Gamma$ and p_1 both lie on the same isochron, they have the same asymptotic phase to γ_0. The point p_2 lies on a different isochron and, hence, has a different asymptotic phase. Figure 1(b) shows the time series of the y-variable of each of the trajectories and illustrates how $\varphi^t(\gamma_0)$ and $\varphi^t(p_1)$ clearly synchronize, whilst $\varphi^t(p_2)$ remains out of phase with a fixed phase difference.

There has recently been a renewed interest in isochrons. Guckenheimer and Sherwood [26] study the phase response of a three-dimensional Hindmarsh-Rose model, which models a bursting neuron. They consider the system near a homoclinic point, and, via a singular-perturbation reduction, compute the isochrons of the two-dimensional fast subsystem. In [19], Mauroy *et al.* extend the work by Guckenheimer and Sherwood by computing the two-dimensional isochrons of the full Hindmarsh-Rose system via their method based on the concept of Fourier averages of observables along trajectories [17]. In [18] Mauroy and Mezić consider systems that exhibit isochrons with fractal geometry, and show that such geometry leads to a very sensitive phase response. In [20], Moehlis considers the geometry of the isochrons for the planar Hopf normal form oscillator and the Hindmarsh-Rose oscillator to understand fluctuations in the periods of oscillators with noise, and how perturbations to regions of diffuse isochrons can reduce such fluctuations. In [2] Castejón *et al.* use isochrons to create phase-response functions and amplitude-response functions, in order to investigate perturbations that lead to transient behavior. Nakao *et al.* [22] generalize the notion of an isochron in order to study phase response in reaction-diffusion-type systems. Sabatini [25] considers isochrons from a more theoretical point of view. He studies isochrons of centers, whether isochrons exist and their associated properties via linearizations and normalizations; he also considers the problem of constructing a system for which the isochrons are a chosen foliation of curves. In [11], Huguet and Guillamon compute isochrons by solving a functional equation for the parameterization of the periodic orbit and its isochrons. More recently, in [13], Huguet and de la Llave extend this parameterization method such that the functional equation can be solved efficiently with Newton's method.

Complicated turns with high curvature have been observed along isochrons. These turns were first observed in the slow-fast two-dimensional reduced Hodgkin-Huxley oscillator [23], where Osinga and Moehlis referred to them as "boomerang turns." In [16] we showed that such sharp turns also exist along isochrons of the slow-fast FitzHugh-Nagumo model. In both of these example models, the oscillators are examples of relaxation oscillations, which are oscillators that exhibits fast and slow segments; these will be discussed in more detail in

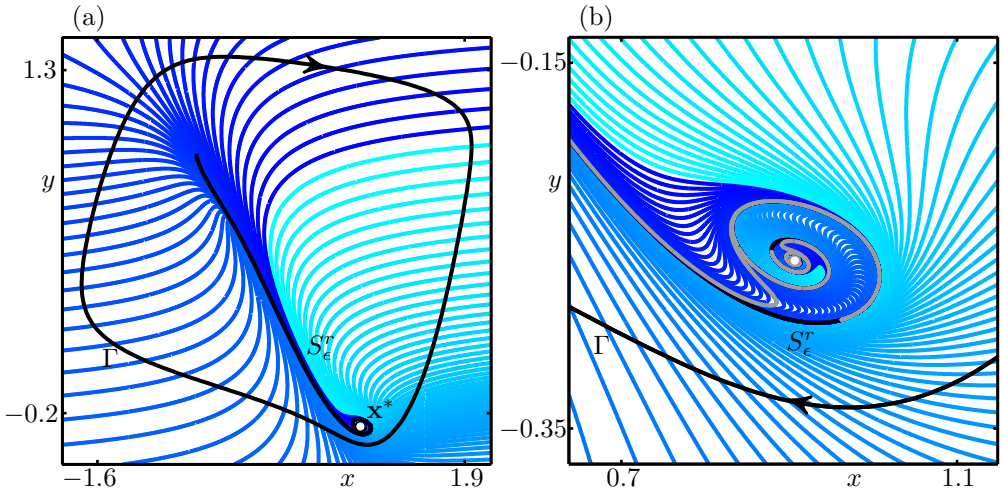

Figure 2: Panel (a) shows one hundred isochrons of the FitzHugh-Nagumo model (8) for $c = 3$. The isochrons are associated with the attracting periodic orbit Γ and are uniformly distributed in phase; the repelling slow manifold S^r_ε is also shown. Panel (b) shows an enlargement near the equilibrium $\mathbf{x}^*$, where the isochron $I(\gamma_{0.8})$ is highlighted in grey.

Section 5.3. Figure 2(a) shows one hundred isochrons for the periodic orbit Γ (black) in the FitzHugh-Nagumo model; for more details on the model see Section 4. The isochrons are uniformly distributed in phase and accumulate on a repelling equilibrium $\mathbf{x}^*$. Again, each isochron has a unique color that determines its phase as given by the color bar in Fig. 1. Figure 2(b) shows an enlargement of a region near the equilibrium $\mathbf{x}^*$, where one particular isochron is emphasized in grey. As the isochron approaches $\mathbf{x}^*$, it periodically undergoes very sharp turns, and appears to go back over itself.

Note that the complicated isochrons in Fig. 2 are topologically the same as the rotationally symmetric, spiraling isochrons in Fig. 1, which do not exhibit sharp turns. We are interested here in what the mechanisms are that lead to the creation of sharp turns.

As for the reduced Hodgkin-Huxley oscillator in [23], there exists a curve in the FitzHugh-Nagumo system near which the isochrons accumulate very tightly. This curve is a repelling slow manifold, labelled S^r_ε, and shown in black in Fig. 2. The repelling slow manifold is a curve, on which points evolve for $O(1)$ duration on the slow time scale before leaving S^r_ε rapidly along the fast direction [8]; here, S^r_ε corresponds to a segment of a special trajectory along which the flow is much slower than in the rest of phase space. Since the slow manifold arises from a time-scale separation in the system, it seems natural to assume that the creation of sharp turns is a feature of systems that exhibit multiple time scales. Indeed, we argued in [16] that the presence of a slow manifold causes the creation of sharp turns.

In this paper we investigate this hypothesis in more detail and argue that the presence of a repelling slow manifold is neither sufficient nor necessary. The central idea is to introduce the notion of backward-time isochrons of a repelling periodic orbit and consider the interactions of foliations of both forward-time and backward-time isochrons. Backward-time isochrons are the (forward-time) isochron of the reverse-time system for which the repelling periodic orbit is attracting. We also generalize these definitions to isochrons of equilibria with complex-conjugate eigenvalues in planar systems. We look at the interactions of the two foliations of isochrons as we vary the vector field. We observe the isochrons curving, and eventually the isochrons have such curvature that they form cubic tangencies, which can be interpreted as to the moment sharp turns are created. In this way, sharp turns are well defined and their creation is a bifurcation in the system, which we call the *cubic isochron foliation tangency* (CIFT) bifurcation. Before the bifurcation, the two foliations of isochrons intersect only transversally, and after the bifurcation, the two foliations of isochrons have non-transverse quadratic intersections.

The paper is organized as follows. In Section 2, we introduce definitions of forward-time and backward-time isochrons for periodic orbits and equilibria. This section is followed, in Section 3, with an example and a brief description of the numerical methods we use. In Section 4, we present the CIFT bifurcation in the FitzHugh-Nagumo model. We describe the unfolding of a generic CIFT bifurcation, and show that the tangent points on the isochrons form trajectories of the dynamical system. In Section 5, we address the question how a CIFT bifurcation can be generated. We construct two different vector fields; the first model creates a CIFT bifurcation via the introduction of a global time-scale separation between the two variables; the second model illustrates that it suffices to slow down the trajectories only in a local region of phase space. As a third mechanism we consider the isochrons in a canard explosion in the Van der Pol system. We end with concluding remarks in Section 6.

2 Setting and definitions

We consider an autonomous n-dimensional vector field of the form

$$\frac{d\mathbf{x}}{dt} = \mathbf{F}(\mathbf{x}), \tag{1}$$

where $\mathbf{F}$ is sufficiently smooth and induces a flow $\varphi : \mathbb{R}\times\mathbb{R}^n \to \mathbb{R}^n$, such that after time $t \in \mathbb{R}$, the point $\mathbf{x}_0 \in \mathbb{R}^n$ is at the point $\varphi(t, \mathbf{x}_0) \in \mathbb{R}^n$; we also use the equivalent notation $\varphi^t(\mathbf{x}_0) = \varphi(t, \mathbf{x}_0)$. We assume that (1) has a hyperbolic periodic orbit Γ with period T_Γ, meaning that only the trivial Floquet multiplier equal to 1 lies on the unit circle of the complex plane. We choose a reference point $\gamma_0 \in \Gamma$ (a typical choice is the maximum with respect to a variable) and define points $\gamma_\theta = \varphi(\theta T_\Gamma, \gamma_0)$ on Γ according to their (unique) phase $\theta = [0, 1)$; here, γ_0 has zero phase.

2.1 Isochrons of an attracting periodic orbit

When Γ is an attracting periodic orbit, its $n-1$ non-trivial Floquet multipliers all lie inside the unit circle and correspond to stable directions. In this case, Γ has an n-dimensional basin of attraction defined as

$$\mathcal{A}(\Gamma) = \{\mathbf{x} \in \mathbb{R}^n \mid \varphi(t, \mathbf{x}) \to \Gamma,\ t \to \infty\},$$

which consists of all points that converge to Γ in forward time. This is the setup that Winfree considered in [28] to introduce the notion of asymptotic phase for planar systems, which is defined as follows. The unique (forward-time) asymptotic phase $\theta_{\mathrm{s}}(\mathbf{x}_0)$ of a point $\mathbf{x}_0 \in \mathcal{A}(\Gamma)$ is given implicitly as

$$\lim_{t\to\infty} |\varphi(t,\, \mathbf{x}_0) - \varphi(t + \theta_{\mathrm{s}}(\mathbf{x}_0)T_\Gamma,\, \gamma_0)| = 0.$$

Hence, the trajectory starting from $\mathbf{x}_0$ asymptotically converges to Γ (in forward time) such that it will be in phase with the trajectory that is initially at $\varphi(\theta_{\mathrm{s}}(\mathbf{x}_0)T_\Gamma,\, \gamma_0) \in \Gamma$.

A (forward-time) isochron of Γ is a level set of the asymptotic phase function

$$\theta_{\mathrm{s}} : \mathcal{A}(\Gamma) \to [0, 1).$$

Each point $\gamma \in \Gamma$ corresponds to a unique isochron, namely,

$$I(\gamma) = \{\mathbf{x}_0 \in \mathcal{A}(\Gamma) \mid \theta_{\mathrm{s}}(\mathbf{x}_0) = \theta_{\mathrm{s}}(\gamma)\}.$$

Guckenheimer [10] views the (forward-time) isochron $I(\gamma)$ of the point $\gamma \in \Gamma$ as the stable manifold of the fixed point γ associated with the map $\varphi^{T_\Gamma}(\cdot)$. By relating isochrons to stable manifolds, it is possible to give rigorous existence and smoothness results. Namely, the Stable Manifold Theorem [12] ensures that $I(\gamma)$ is tangent at γ to the stable eigenspace spanned by the $n-1$ eigenvectors that correspond to the $n-1$ Floquet multipliers of the $n \times n$ Jacobian matrix $D\varphi^{T_\Gamma}(\gamma)$ at the point $\gamma \in \Gamma$; hence, each isochron is transverse to Γ at γ. By

definition, each isochron maps to another under the time-Δt map, that is, the isochrons are the diffeomorphic images of each other under the flow of (1). Hence, the set of all isochrons

$$\mathcal{I}(\Gamma) = \{I(\gamma) | \gamma \in \Gamma\} \tag{2}$$

is a foliation of the basin of attraction $\mathcal{A}(\Gamma)$ over Γ with leaves $I(\gamma)$.

The problem of existence of asymptotic phase for non-hyperbolic periodic orbits in planar systems has been addressed by Chicone and Liu [3]. They also provide a different proof of the existence of asymptotic phase for hyperbolic periodic orbits. Dumortier extended their result and proved that, as a consequence of asymptotic phase, a foliation as smooth as the vector field must exist, which is made up of leaves that transversally intersect the periodic orbit [7].

2.2 Isochrons of a repelling periodic orbit

We now introduce the concept of a backward-time isochron $U(\gamma)$ for a repelling periodic orbit Γ. In this case Γ has an n-dimensional basin of repulsion defined as the set

$$\mathcal{R}(\Gamma) = \{\mathbf{x} \in \mathbb{R}^n \mid \varphi(t, \mathbf{x}) \to \Gamma,\ t \to -\infty\}$$

of points that converge to Γ in backward time.

In the case of backward-time isochrons of a repelling periodic orbit Γ, the arguments used in Section 2.1 can be applied trivially by reversing time. Specifically, each backward-time isochron $U(\gamma)$ is the unstable manifold of the time-(T_Γ) map $\varphi^{T_\Gamma}(\cdot)$. Consequently, the Stable Manifold Theorem [12] ensures that each isochron $U(\gamma)$ is tangent to the unstable linear eigenspace that is spanned by the $n-1$ unstable eigenvectors of the Jacobian matrix $D\varphi^{T_\Gamma}(\cdot)$ evaluated at γ. Each backward-time isochron is also everywhere transverse to the flow and is the diffeomorphic image of the other backward-time isochrons under the flow. Hence, as before, the set of all backward-time isochrons

$$\mathcal{U}(\Gamma) = \{U(\gamma) \mid \gamma \in \Gamma\} \tag{3}$$

is a foliation of the basin $\mathcal{R}(\Gamma)$ over Γ with leaves $U(\gamma)$.

2.3 Isochrons of a saddle periodic orbit

When Γ is a saddle periodic orbit, k of the $n-1$ non-trivial Floquet multipliers lie inside and $n-(k+1)$ Floquet multipliers lie outside the unit circle. In this case, Γ has a $(k+1)$-dimensional stable manifold W^s, which is the set of points that converge to Γ in forward time, and an $(n-k)$-dimensional unstable manifold W^u, which is the set of points that converge to Γ in backward time. The definition of a stable manifold W^s agrees with the definition of the basin of attraction for the case of isochrons of an attracting periodic orbit. Similarly, the definition of an unstable manifold W^u agrees with the definition of the basin of repulsion for the case of isochrons of a repelling periodic orbit. As a consequence, there is a foliation on each of the two manifolds [12], which can be considered as the set of forward-time or backward-time isochrons and the properties discussed in the above two sections apply.

2.4 Isochrons of spiraling equilibria in planar systems

A focus equilibrium $\mathbf{x}^*$ has complex-conjugate eigenvalues and, hence, an associated rotation. We use this rotation to define a set of isochrons associated with $\mathbf{x}^*$, which extends the notion of an isochron to focus equilibria. In higher-dimensional systems, there may be multiple pairs of complex-conjugate eigenvalues so that the set of isochrons for $\mathbf{x}^*$ is not unique. Here, we are interested in the case of planar systems for which $\mathbf{x}^*$ has a single pair of complex-conjugate eigenvalues; in this case, we can apply results from the literature. Isochrons for an equilibrium of a planar vector field are also known as isochronous sections. Sabatini [24, Definition 2] introduced the concept of an isochronous section of a focus equilibrium $\mathbf{x}^*$ in a planar system of the form (1). In our notation, an isochronous section is a C^1-curve $\eta : [0, +\infty) \to \mathbb{R}^2$ with $\lim_{s\to\infty} \eta(s) = \mathbf{x}^*$, such that η is invariant under the time-T map for some $T > 0$, but not for any time smaller than T. Sabatini also shows

that (1) has isochronous sections at $\mathbf{x}^*$ if there exists a local diffeomorphism at $\mathbf{x}^*$ such that the system (1) can be written in polar coordinates with non-zero rotation at $\mathbf{x}^*$.

Isochronous sections are not unique and may exist for any choice of T. Sabatini [24] proves the existence of isochronous sections for a particular choice of T, namely for $T = T_{\mathbf{x}^*} = \frac{2\pi}{\beta}$, where β is the imaginary part of the eigenvalues of $\mathbf{x}^*$; we call $T_{\mathbf{x}^*}$ the natural period of $\mathbf{x}^*$. The isochronous sections converge to $\mathbf{x}^*$ radially if T is the natural period of $\mathbf{x}^*$, or an integer multiple of $T_{\mathbf{x}^*}$; otherwise, the isochronous sections will approach $\mathbf{x}^*$ in a spiraling manner, as in Fig. 1. We define the (forward-time and backward-time) isochrons of a focus equilibrium of a planar vector field as the isochronous section associated with the natural period $T = T_{\mathbf{x}^*}$. In this way, the isochrons of a focus equilibrium are the direct generalization of isochrons for periodic orbits by way of a polar blow-up in $\mathbb{R}^2$ [1].

2.5 The CIFT bifurcation in planar systems

We are interested in what happens when forward-time and backward-time isochrons interact. To this end, we consider the setting of planar systems from now on, and assume that there exists a region where foliations by both forward-time and backward-time isochrons exist. We consider two settings: in the first case, there is an attracting periodic orbit Γ_s surrounding a repelling periodic orbit Γ_u that lies on the basin boundary of Γ_s; in the second case, the attracting periodic orbit Γ_s encloses a repelling equilibrium $\mathbf{x}^*$. For each case, there exist forward-time isochrons with an associated period T_s, and backward-time isochrons with an associated (natural) period T_u. The isochron foliations $\mathcal{I}(\Gamma_\mathrm{s})$ and $\mathcal{U}(\Gamma_\mathrm{u})$ (or $\mathcal{U}(\mathbf{x}^*)$) coexist in the annulus bounded by Γ_s and Γ_u (or $\mathbf{x}^*$).

If Γ_s and Γ_u (or $\mathbf{x}^*$) have the same period, that is, $T_\mathrm{s} = T_\mathrm{u}$, then the two forward-time and backward-time isochron foliations are identical in the annulus; this is a maximally degenerate situation. In general, there exists a parameter regime such that the isochrons intersect in one of the following two possibilities:

(*G1*). The two foliations $\mathcal{I}(\Gamma_\mathrm{s})$ and $\mathcal{U}(\Gamma_\mathrm{u})$ (or $\mathcal{U}(\mathbf{x}^*)$) are everywhere transverse to each other. That is, any intersection between a forward-time isochron $I(\gamma^\mathrm{s})$ and a backward-time isochron $U(\gamma^\mathrm{u})$ is transverse.

(*G2*). The two foliations $\mathcal{I}(\Gamma_\mathrm{s})$ and $\mathcal{U}(\Gamma_\mathrm{u})$ (or $\mathcal{U}(\mathbf{x}^*)$) are non-transverse. That is, at least one forward-time isochron $I(\gamma^\mathrm{s})$ and one backward-time isochron $U(\gamma^\mathrm{u})$ do not intersect transversally but have a tangency; generically, such tangencies are quadratic. The points of tangency occur along particular trajectories, which accumulate on Γ_s in forward and Γ_u (or $\mathbf{x}^*$) in backward time.

These two generic situations are structurally stable, that is, properties (*G1*) and (*G2*) are not destroyed under small variation of the vector field. Hence, the transition from one to another yields a bifurcation of the two foliations; we call this a *cubic isochron foliation tangency (CIFT) bifurcation.* At a CIFT bifurcation, the two foliations $\mathcal{I}(\Gamma_\mathrm{s})$ and $\mathcal{U}(\Gamma_\mathrm{u})$ (or $\mathcal{U}(\mathbf{x}^*)$) are non-transverse in such a way that at least one forward-time isochron and one backward-time isochron have a higher-order tangency; generically, this tangency is cubic. There exists a single corresponding trajectory O^* along which points of cubic tangency occur; O^* accumulates on Γ_s in forward and Γ_u (or $\mathbf{x}^*$) in backward time.

At a CIFT bifurcation, two trajectories $O^\pm$ are created from the special trajectory O^* and the CIFT bifurcation can be seen as a fold bifurcation that gives rise to the two trajectories $O^\pm$ along which the two foliations are (quadratically) tangent. We remark that further CIFT bifurcations can occur in parameter regime (*G2*) giving rise to more tangencies between the two foliations.

The trajectories O^* and $O^\pm$ pass through each isochron in both foliations. Hence, in the non-transverse regime (*G2*), all isochrons in the foliations have a tangency. We can map the point of tangency between a forward-time isochron $I(\gamma^\mathrm{s})$ and a backward-time isochron $U(\gamma^\mathrm{u})$, together with the isochrons themselves, forward and backward in time under the flow to points of tangency between other forward-time and backward-time isochrons. At integer multiples mT_s, $m \in \mathbb{Z}$, of the period of T_s, the point of tangency returns to $I(\gamma^\mathrm{s})$, and at these points there are tangencies between $I(\gamma^\mathrm{s})$ and other backward-time isochrons. The time mT_s corresponds to a phase shift of $m\frac{T_\mathrm{s}}{T_\mathrm{u}}$ (mod 1). Hence, the set of backward-time isochrons $\{U(\gamma^\mathrm{u}_\vartheta) \mid \vartheta = (\theta_\mathrm{u}(\gamma^\mathrm{u}) + m\frac{T_\mathrm{s}}{T_\mathrm{u}}) \text{ (mod 1)}, m \in \mathbb{Z}\}$ forms a tangency with $I(\gamma^\mathrm{s})$. If the ratio of periods $\frac{T_\mathrm{s}}{T_\mathrm{u}}$ is rational, then this set is finite; conversely, if this ratio is irrational, then the set is infinite. With the same reasoning, at integer multiples of the period of Γ_u the point of tangency returns to $U(\gamma^\mathrm{u})$, and at these points there are tangencies between $U(\gamma^\mathrm{u})$ and the set of forward-time isochrons $\{I(\gamma^\mathrm{s}_\vartheta) \mid \vartheta = (\theta_\mathrm{s}(\gamma^\mathrm{s}) + m\frac{T_\mathrm{u}}{T_\mathrm{s}}) \text{ (mod 1)}, m \in \mathbb{Z}\}$.

We stress that throughout both the foliation $\mathcal{I}(\Gamma_s)$ and the foliation $\mathcal{U}(\Gamma_u)$ remain transverse to all orbits of the vector field regardless of whether they are non-transverse to each other or not.

2.6 Computation of isochrons

Both the forward-time and backward-time isochrons of periodic orbits are computed with the method presented in [16] for planar systems. Each forward-time (backward-time) isochron is computed as the stable (unstable) manifold of the time-T_s (time-T_u) map of the associated point on the periodic orbit, represented by a single parameterized curve. We adapt this method to compute the isochrons of equilibria with complex-conjugate eigenvalues. Here, we briefly discuss the method and focus on the adaptation used to compute a backward-time isochron $U(\mathbf{x}^*_\theta)$ of an equilibrium $\mathbf{x}^*$; we refer to [16] for full details.

The main difference between computing isochrons of a periodic orbit and those of an equilibrium is the construction of a local approximation. For a periodic orbit, this local linear approximation is found by determining its (un)stable linear eigenbundle, as described in [14]. The linear approximation of an isochron $U(\mathbf{x}^*_\theta)$ of an equilibrium $\mathbf{x}^*$ is given by a line from $\mathbf{x}^*$ in a particular direction. Each direction corresponds to a particular phase, but a uniform distribution of angle does not correspond to a uniform distribution of phase, which depends on the linearized system at $\mathbf{x}^*$. The Jacobian matrix $D\mathbf{F}$ at $\mathbf{x}^*$ has complex-conjugate eigenvalues $\mu = \alpha \pm \beta i$ and corresponding complex-conjugate eigenvectors $\mathbf{w}, \overline{\mathbf{w}} \in \mathbb{C}^2$. Hence, the trajectories of the linearized system about $\mathbf{x}^*$ are of the form

$$\hat{\mathbf{x}}(t) = \{\mathbf{x}^* + c\mathbf{w}e^{(\alpha+\beta i)t} + \overline{c\mathbf{w}}e^{(\alpha-\beta i)t} \,|\, 0 \le t < T_{\mathbf{x}^*}\},$$

where $T_{\mathbf{x}^*} = \frac{2\pi}{\beta}$ is the natural period of $\mathbf{x}^*$, and the coefficient $c \in \mathbb{C}$ defines the initial point $\hat{\mathbf{x}}(0) \in \mathbb{R}^2$. We write this rotation about $\mathbf{x}^*$ in terms of an amplitude and a phase, so that we obtain the more convenient form

$$\hat{\mathbf{x}}(t) = \{\mathbf{x}^* + \mathbf{c_1}e^{\alpha t}\cos(\beta t + \mathbf{c_2}) \,|\, 0 \le t < T_{\mathbf{x}^*}\}, \tag{4}$$

where $\mathbf{c_1} = 2\text{abs}(\overline{c\mathbf{w}}) \in \mathbb{R}^2$ and $\mathbf{c_2} = \text{angle}(\overline{c\mathbf{w}}) \in \mathbb{R}^2$. Note that we abused notation here and equation (4) should be interpreted component-wise as is standard in Matlab; in particular, $\mathbf{c_1}$ and $\mathbf{c_2}$ are the component-wise norm and argument of $\overline{c\mathbf{w}}$, respectively, and the cosine function is vector valued.

In the absence of growth or decay, that is, if $\alpha = 0$, the linearized system (4) traces out an ellipse $D = \{\mathbf{x}^* + \mathbf{c_1}\cos(\beta t + \mathbf{c_2}) \,|\, 0 \le t < T_{\mathbf{x}^*}\}$, which represents the rotation near $\mathbf{x}^*$. For $||\mathbf{c_1}||$ small enough, the ellipse D is a good approximation of the trajectory segment $\hat{\mathbf{x}}(t)$ and, thus, of the phase distribution near $\mathbf{x}^*$. We now choose $c \in \mathbb{C}$, and consequently $\mathbf{c_1}, \mathbf{c_2} \in \mathbb{R}^2$, such that $\hat{\mathbf{x}}(0)$ is the point on D with maximal x-value. As is customary for periodic orbits, the normalized vector $\mathbf{v}_0$ through $\mathbf{x}^*$ and $\hat{\mathbf{x}}(0)$ defines the linear approximation of the isochron associated with zero phase. For any other given phase θ, the corresponding linear approximation is given by the normalized vector $\mathbf{v}_\theta$ through $\mathbf{x}^*$ and the point $\hat{\mathbf{x}}(\theta T_{\mathbf{x}^*}) = \mathbf{x}^* + \mathbf{c_1}\cos(\beta\theta T_{\mathbf{x}^*} + \mathbf{c_2})$ on D.

We restrict the length of the linear approximation to a pre-specified maximum length $\eta_{\max}$. Hence, the local linear approximation of the isochron $U(\mathbf{x}^*_\theta)$ is given by the line segment $R_\theta = \{R_\theta(\eta) := \mathbf{x}^* + \eta\mathbf{v}_\theta \,|\, 0 \le \eta \le \eta_{\max}\}$ from $\mathbf{x}^*$ extending $\eta_{\max}$ in the direction $\mathbf{v}_\theta$. Provided $\eta_{\max} \ll 1$, the line segment R_θ is a good local approximation of $U(\mathbf{x}^*_\theta)$.

To compute the global isochron $U(\mathbf{x}^*_\theta)$, we extend the local linear approximation by including the initial points of orbit segments that end on R_θ after (integer multiples of) the natural period $T_{\mathbf{x}^*}$ of $\mathbf{x}^*$. Such orbit segments are η-dependent families that can be computed via continuation, for which we use the continuation package AUTO [6]. The setup in AUTO is as follows. We first rescale the vector field (1) to

$$\dot{\mathbf{u}} = T\mathbf{F}(\mathbf{u}), \tag{5}$$

where we set $T = -T_{\mathbf{x}^*}$, such that an orbit segment $\mathbf{x} := \{\mathbf{x}(t) \mid -T_{\mathbf{x}^*} < t < 0\}$ of (1) corresponds to the orbit segment $\mathbf{u} := \{\mathbf{u}(t) \mid 0 < t < 1\}$ of (5). We impose the boundary condition

$$\mathbf{u}(1) = R_\theta(\eta), \tag{6}$$

which constrains the end point $\mathbf{u}(1)$ to the linear approximation R_θ, namely a point at distance η from $\mathbf{x}^*$. Hence, (5) and (6) define a unique family of orbit segments that is parameterized by η. The initial points $\mathbf{u}(0)$ of the orbit segments form a new portion of $U(\mathbf{x}^*_\theta)$.

The solution $\mathbf{u} \equiv \mathbf{x}^*$ with $\eta = 0$ is a known solution to the boundary value problem (5) and (6). We compute the family of orbit segments by continuing this known solution in η, up to the maximum tolerance $\eta = \eta_{\max}$. We can extend $U(\mathbf{x}_\theta^*)$ further by considering points that map to R_θ after successive integer multiples of $T_{\mathbf{x}^*}$. That is, we seek solutions to the boundary value problem (5) and (6) but with integration times $T = -kT_{\mathbf{x}^*}$, where $k = 2, 3$, and so on. With this setup, we can extend $U(\mathbf{x}_\theta^*)$ up to any desired arclength.

Near a non-hyperbolic equilibrium, such as at a Hopf bifurcation, which we discuss in Section 4.3, the expansion or contraction to the equilibrium is polynomial rather than exponential at the non-hyperbolic point. Hence, as the end point of an orbit segment moves along the linear approximation, the initial point of the orbit segment only moves an almost equally small distance, which results in only a small extension to the isochron. In this situation, one needs to compute a larger extension by repeating the continuation for orbit segments with successively larger integer multiples of $T_{\mathbf{x}^*}$; this requires impractically long orbit segments. A remedy is to allow for a large $\eta_{\max}$.

3 Winfree's model

We illustrate the organization of forward-time and backward-time isochrons by considering the simple model introduced by Winfree [29], given in polar coordinates by:

$$\begin{cases} \dot{r} &= (1-r)(r-a)r, \\ \dot{\psi} &= -(1+\omega(1-r)). \end{cases}$$

In Euclidean coordinates, the system is

$$\begin{cases} \dot{x} &= f_1(x,y) &= (1-\sqrt{x^2+y^2})\left(x\,(\sqrt{x^2+y^2}-a)+\omega y\right)+y, \\ \dot{y} &= f_2(x,y) &= (1-\sqrt{x^2+y^2})\left(y\,(\sqrt{x^2+y^2}-a)-\omega x\right)-x, \end{cases} \tag{7}$$

where $0 \le a < 1$ and $\omega < 0$. System (7) has the unit circle as an attracting periodic orbit $\Gamma_{\rm s}$ with period $T_{\rm s} = 2\pi$. The origin is an equilibrium $\mathbf{x}^*$. It is attracting for $0 < a < 1$, in which case there also exists a repelling periodic orbit $\Gamma_{\rm u}$, namely, the circle $r = a$ with period $T_{\rm u} = \frac{2\pi}{(1+\omega(1-a))}$. For $a = 0$, the point $\mathbf{x}^*$ is non-hyperbolic and weakly repelling, but the rotation at $r = 0$ in (7) is non-zero. Hence, isochrons of $\mathbf{x}^*$ exist [24]. In this case, the eigenvalues of $\mathbf{x}^*$ are $\mu = \pm\frac{i}{2}$, so that its natural period is $T_{\mathbf{x}^*} = 4\pi$. We fix $\omega = -0.5$ and consider two cases: we choose $a = 0.25$ as a representative value for the case when $\Gamma_{\rm u}$ exists, and $a = 0$ for the case where there is only one periodic orbit, which is also the example shown in Fig. 1.

Figure 3 shows isochrons of (7) for the case $a = 0.25$ (left column) and for $a = 0$ (right column). We plot the unit circle $\Gamma_{\rm s}$, the equilibrium $\mathbf{x}^*$ at the origin and also include the circle $r = 0.25$ for $\Gamma_{\rm u}$ in the left column. In both cases, row (a) shows ten forward-time isochrons of $\Gamma_{\rm s}$; see also Fig. 1(a). The isochrons are uniformly distributed in phase, where their phases are measured relative to the point $\gamma_0^{\rm s} := (x, y) = (1, 0)$ with zero phase as indicated by the color bar. The isochrons accumulate on $\Gamma_{\rm u}$ in panel (a1) and on $\mathbf{x}^*$ in panel (a2). Row (b) shows ten backward-time isochrons for $\Gamma_{\rm u}$ and $\mathbf{x}^*$ in panels (b1) and (b2), respectively. In panel (b1), the point $\gamma_0^{\rm u} := (x, y) = (0.25, 0)$ is assigned zero phase, and in panel (b2), the direction of zero phase is chosen to be $\mathbf{v}_0 = [1, 0]^{\rm T}$. Again, these isochrons are uniformly distributed in phase, where their phases are indicated by the color bar in row (b). In both panels (b1) and (b2) the isochrons accumulate on $\Gamma_{\rm s}$ and on $\mathbf{x}^*$. We use $\eta_{\max} = 10^{-6}$ for the computation of the isochrons of both $\Gamma_{\rm s}$ and $\Gamma_{\rm u}$, and $\eta_{\max} = 10^{-2}$ for the computation of the isochrons of $\mathbf{x}^*$ in Fig. 3(b2). Row (c) shows both sets of forward-time and backward-time isochrons in one figure. The isochrons coexist in the annulus bounded by $\Gamma_{\rm s}$ and $\Gamma_{\rm u}$ in panel (c1), and the punctured disk excluding $\mathbf{x}^*$ in panel (c2). Observe that the two isochron sets intersect each other transversally, which illustrates that the two foliations (and also the example in Fig. 1) satisfy condition (*G1*) of Section 2.5.

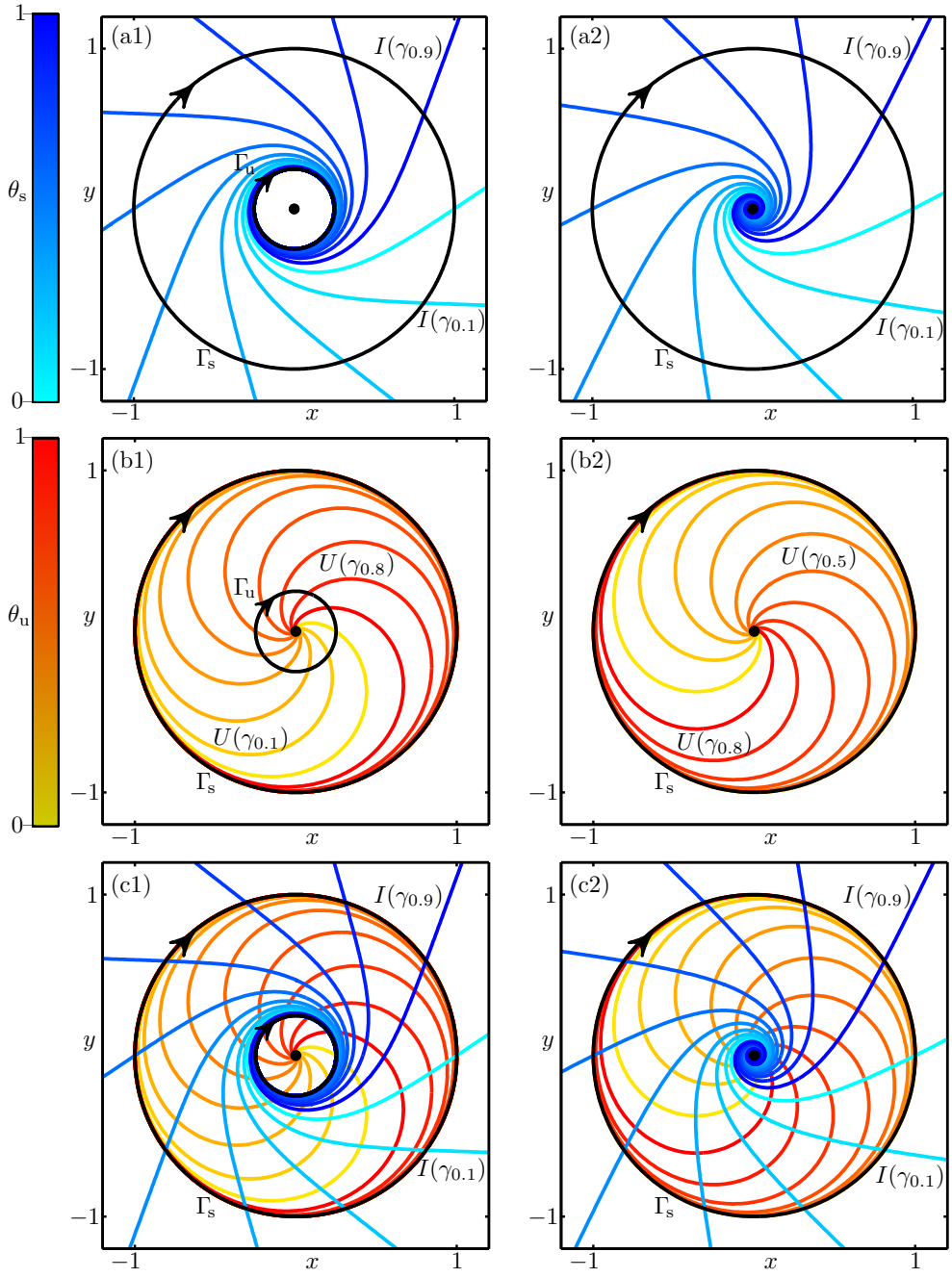

Figure 3: Isochrons of (7) with $a = 0.25$ in the left column where both periodic orbits Γ_s and Γ_u exist, and $a = 0$ in the right column where only Γ_s exists. Row (a) shows ten forward-time isochrons of Γ_s. Row (b) shows ten backward-time isochrons of the repelling periodic orbit Γ_u (b1) and the repelling equilibrium $\mathbf{x}^*$ (b2). Row (c) shows both sets of isochrons together. The isochrons are uniformly distributed in phase and colored according to their phases as indicated by the color bars.

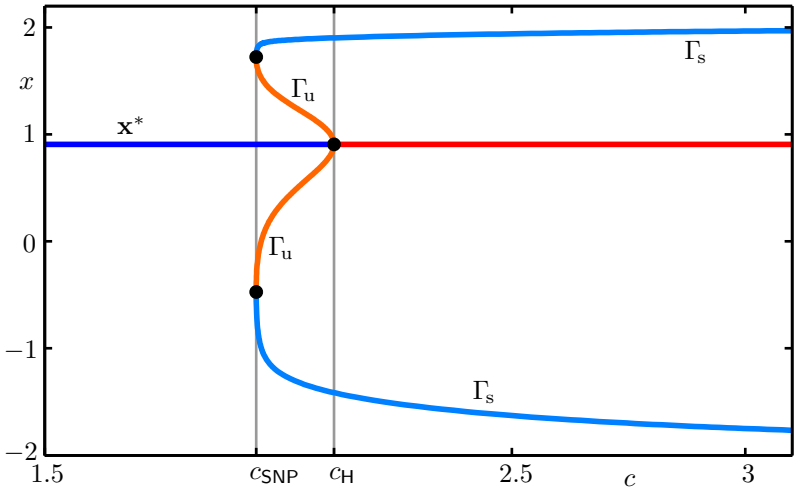

Figure 4: One-parameter bifurcation diagram in the (c, x)-plane of the FitzHugh-Nagumo model (8), showing the equilibrium $\mathbf{x}^*$ and maximum and minimum x-values of the branch of attracting periodic orbits Γ_{s} and the repelling periodic orbits Γ_{u} emanating from the Hopf bifurcation at $c_{\mathsf{H}} \approx 2.1192$. The two branches meet at a saddle-node bifurcation of periodic orbits at $c_{\mathsf{SNP}} \approx 1.9527$; blue curves correspond to attractors and red curves to repellers.

4 Interactions of forward-time and backward-time isochrons in the FitzHugh-Nagumo model

In this section we show that there is a CIFT bifurcation in the planar FitzHugh-Nagumo model [9], a model that was suggested as a description of an excitable system such as a neuron. It is a typical planar slow-fast system with a cubic-shaped nullcline, which gives rise to relaxation oscillations for a sufficiently large time-scale separation. The FitzHugh-Nagumo model is given by the equations

$$\begin{cases} \dot{x} &= c\left(y + x - \dfrac{x^3}{3} + z\right), \\ \dot{y} &= -\dfrac{x - a + by}{c}. \end{cases} \tag{8}$$

Winfree used this model with $a = 0.7$, $b = 0.8$, $c = 3$ and $z = -0.4$ as an example to illustrate the newly introduced concept of a (forward-time) isochron [29]. Due to intrinsic sensitivity in the system he could not fully resolve the isochrons. As we showed in [16], our method of computing isochrons via the continuation of solutions to a two-point boundary value problem is able to resolve the isochrons of the FitzHugh-Nagumo system fully. We now fix parameters a, b and z to those used by Winfree, and explore how the intersections of forward-time and backward-time isochrons change as we vary the time-scale separation parameter c. For $c^2 > 1$, the variable x evolves on a faster time scale than y. There is an equilibrium at $\mathbf{x}^* \approx (0.9066, -0.2582)$; the parameter c does not influence the location of $\mathbf{x}^*$ but changes its stability properties.

Figure 4 shows a bifurcation diagram of (8) in the (c, x)-plane. The equilibrium $\mathbf{x}^*$ (horizontal line) is attracting (blue) for $c < c_{\mathsf{H}} \approx 2.1192$ and repelling for $c > c_{\mathsf{H}}$. At $c = c_{\mathsf{H}}$, a subcritical Hopf bifurcation occurs and a family of repelling periodic orbits Γ_{u} (red) emanates; only the maximum and minimum x-values of the periodic orbits are plotted in Fig. 4. A family of attracting periodic orbits Γ_{s} exist for all $c > c_{\mathsf{SNP}} \approx 1.9527$. At $c = c_{\mathsf{SNP}}$ the periodic orbits Γ_{s} and Γ_{u} coalesce in a saddle-node bifurcation of periodic orbits. Hence, for $c < c_{\mathsf{SNP}}$, the equilibrium $\mathbf{x}^*$ is the only attractor. We are interested in the parameter range $c > c_{\mathsf{SNP}}$. More specifically, we explore the interaction of the forward-time isochrons of Γ_{s} and the backward-time isochrons of

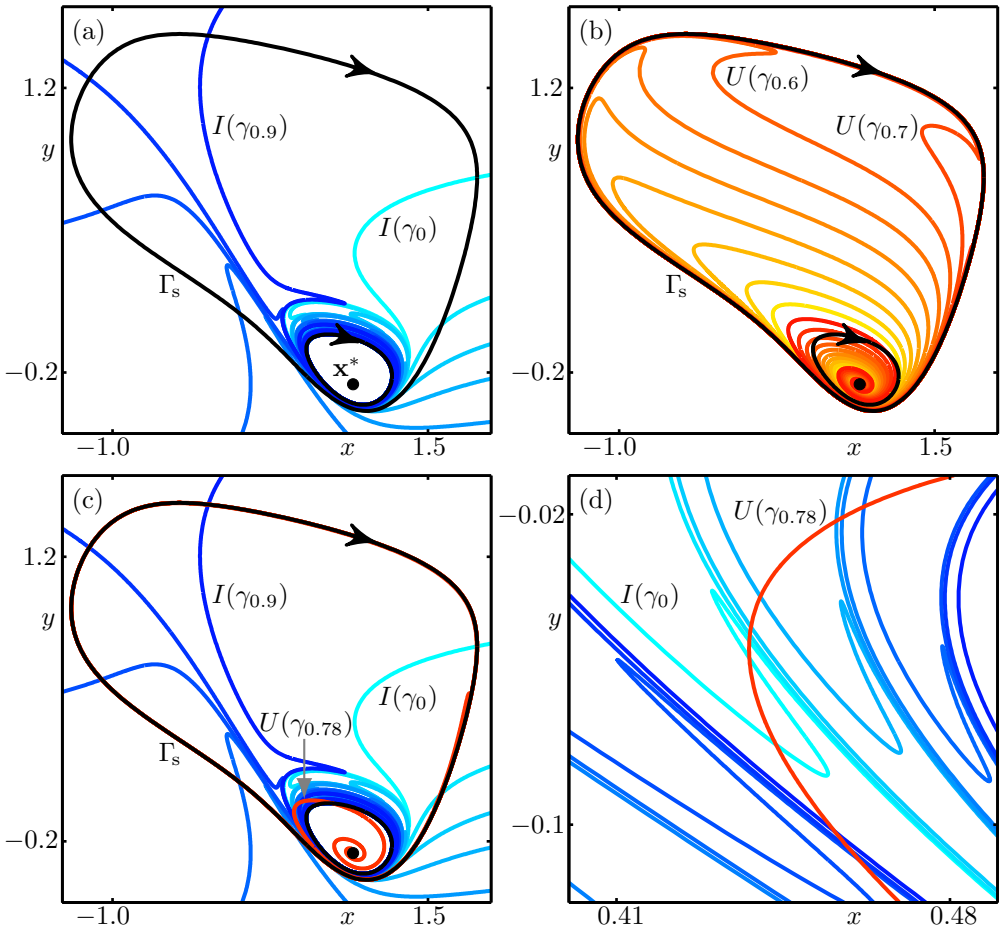

Figure 5: Isochrons of the FitzHugh-Nagumo model (8) for $c = 2.05$. Panel (a) shows ten forward-time isochrons of Γ_s, and panel (b) ten backward-time isochrons of Γ_u. Both sets of isochrons are uniformly distributed in phase. Panel (c) shows the same ten forward-time isochrons from panel (a) with a single backward-time isochron $U(\gamma_{0.78})$; an enlargement near the top left of $U(\gamma_{0.78})$ is shown in panel (d).

Γ_u when $c_{\mathsf{SNP}} < c < c_{\mathsf{H}}$, and the interaction of the forward-time isochrons of Γ_s and the backward-time isochrons of the focus equilibrium $\mathbf{x}^*$ when $c \geq c_{\mathsf{H}}$.

4.1 Local picture of the CIFT bifurcation

If we vary the time-scale separation parameter c, a CIFT bifurcation occurs in the FitzHugh-Nagumo model (8). Figure 5 shows isochrons of (8) for $c = 2.05$. Panel (a) shows ten forward-time isochrons of the attracting periodic orbit Γ_s uniformly distributed in phase. Here, we observe that, as the forward-time isochrons approach Γ_u, they develop high-curvature features as described in [16]. Panel (b) shows ten backward-time isochrons of the periodic orbit Γ_u, again uniformly distributed in phase. Notice similar high-curvature features as the backward-time isochrons approach Γ_s. Here, $T_s \approx 10.98$ and $T_u \approx 7.45$, and the forward-time and backward-time isochrons with zero phase are associated with the points with maximum x on Γ_s and Γ_u, respectively. Panel (c) shows the ten isochrons from panel (a) together with the single backward-time isochron $U(\gamma_{0.78})$. The enlargement in panel (d) illustrates clearly that $U(\gamma_{0.78})$ actually intersects $I(\gamma_0)$ locally three times, while it intersects the other forward-time isochrons shown in this region only once. From Fig. 5(d) we can conclude that

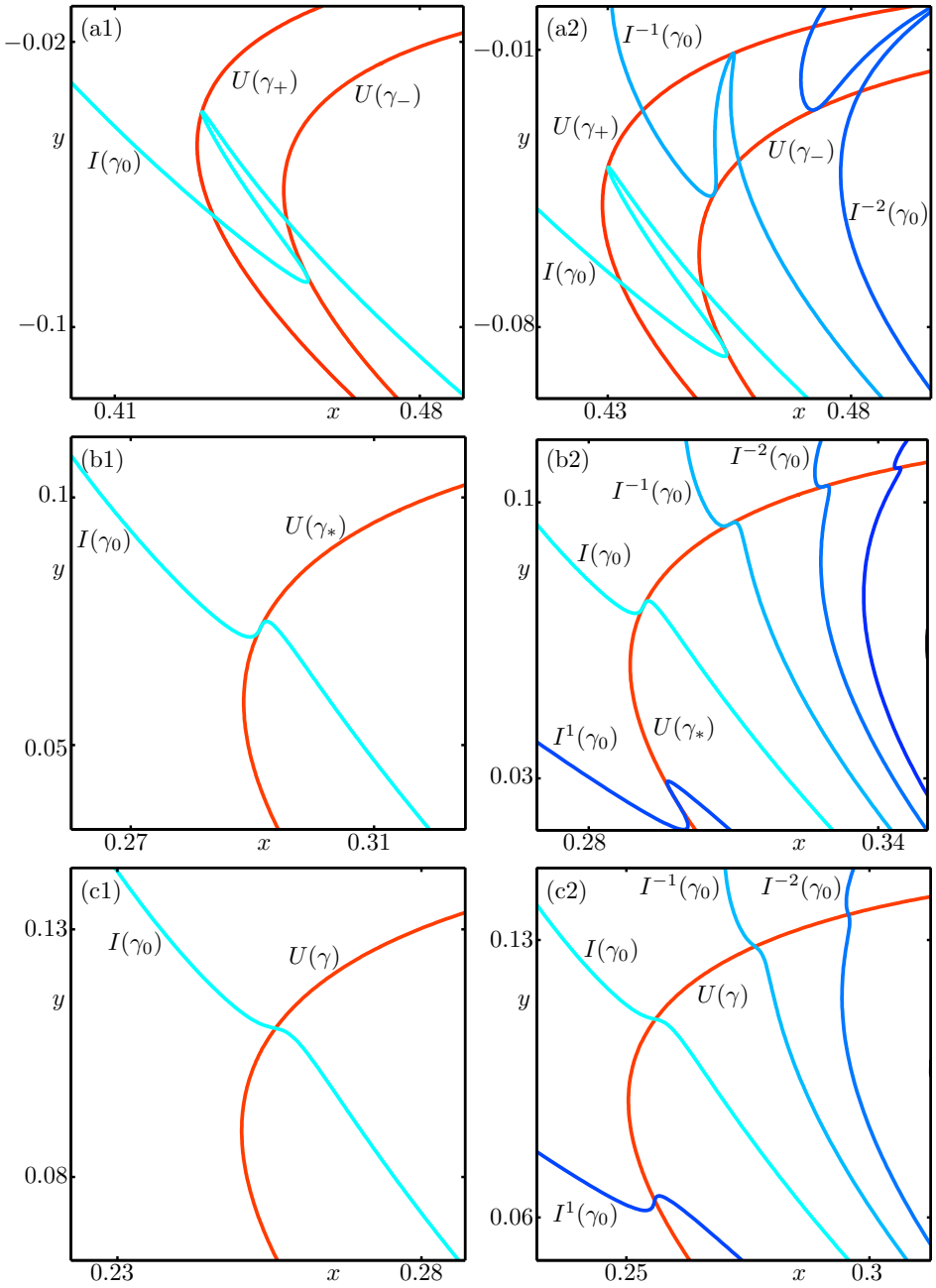

Figure 6: CIFT bifurcation of the forward-time isochron $I(\gamma_0)$ of the FitzHugh-Nagumo model (8); shown are selected forward-time and backward-time isochrons for $c = 2.05$, $c = 2.0071$ and $c = 2$. The left column shows only $I(\gamma_0)$ with backward-time isochrons before, at and after the CIFT bifurcation, that illustrate the transition from two quadratic tangencies through a cubic tangency to a transverse intersection; the right column also shows some isochrons $I^m(\gamma_0)$ that are the images of $I(\gamma_0)$ under the time-T_u map.

there must be two backward-time isochrons near $U(\gamma_{0.78})$ that have quadratic tangencies with $I(\gamma_0)$. Hence, the foliations $\mathcal{I}(\Gamma_s)$ and $\mathcal{U}(\Gamma_u)$ are not transverse for $c = 2.05$.

To investigate how this non-transversality arises we consider isochron interactions as we decrease c. Figure 6

shows enlargements of intersections of $I(\gamma_0)$ and certain backward-time isochrons for $c = 2.05$, $c = 2.0071$ and $c = 2$. Row (a) shows the forward-time isochron $I(\gamma_0)$ for $c = 2.05$ as in Fig. 5, but now with the two backward-time isochrons $U(\gamma_+)$ and $U(\gamma_-)$ that have quadratic tangencies with $I(\gamma_0)$ in this region of the phase plane. Backward-time isochrons to the left of $U(\gamma_+)$, or to the right of $U(\gamma_-)$ intersect $I(\gamma_0)$ only once in the region shown in panel (a1), whereas a backward-time isochron that lies between $U(\gamma_+)$ and $U(\gamma_-)$ locally intersects $I(\gamma_0)$ three times; compare with Fig. 5(d). The points of tangency between $I(\gamma_0)$ and $U(\gamma_+)$ and $U(\gamma_-)$ are mapped under the flow of system (8). Hence, we can find other forward-time isochrons that have quadratic tangencies with $U(\gamma_+)$ and $U(\gamma_-)$, namely, $I^m(\gamma_0) := \varphi(mT_{\rm u}, I(\gamma_0))$ for $m \in \mathbb{Z}$, where $I^0(\gamma_0) = I(\gamma_0)$. In Fig. 6(a2) we show the forward-time isochrons $I^0(\gamma_0)$, $I^{-1}(\gamma_0)$ and $I^{-2}(\gamma_0)$. Figure 6(b1) shows the situation approximately at the moment of the CIFT bifurcation, which occurs at $c \approx 2.0071$. In the region shown, $I(\gamma_0)$ forms a cubic tangency with the single backward-time isochron $U(\gamma_*)$. Panel (b2) shows the five forward-time isochrons $I^m(\gamma_0)$, $m \in \{-3, -2, -1, 0, 1\}$, which have cubic tangencies with $U(\gamma_*)$ near $I(\gamma_0)$. Figure 6(c) shows isochrons for $c = 2$. In panel (c1), we show the backward-time isochron $U(\gamma)$ intersecting $I(\gamma_0)$ transversally. Here, we chose $U(\gamma)$ such that it intersects $I(\gamma_0)$ in roughly the same region as where the CIFT bifurcation occurs locally; this backward-time isochron is not unique, but we selected one that can be viewed as a continuation of $U(\gamma_*)$. Even though system (8) still exhibits a time-scale separation, $I(\gamma_0)$ and all other forward-time isochrons now intersect all backward-time isochrons $U(\gamma)$ transversally. Panel (c2) shows the forward-time isochrons $I^m(\gamma_0)$, $m \in \{-2, -1, 0, 1\}$, that intersect $U(\gamma)$ near $I(\gamma_0)$.

Figure 6 shows the local unfolding of a CIFT bifurcation of $I(\gamma_0)$ as we decrease c. The cubic tangency shown in row (b) separates the parameter regime with non-transverse intersections, illustrated in row (a), from that with only transverse intersections as illustrated in row (c). Note that each of the panels in the right column only show relevant connected parts of the isochrons near the cubic tangency; other transverse intersections occur, which are not shown here, but examples can be seen in Fig. 5(d).

4.2 Global picture of CIFT bifurcation

Figures 7–9 show a series of images before, at and after the CIFT bifurcation, which illustrate how the unfolding of a CIFT bifurcation manifests itself globally in the annulus bound by $\Gamma_{\rm s}$ and $\Gamma_{\rm u}$. Each figure shows 26 forward-time isochrons of $\Gamma_{\rm s}$, which have phases $\theta_j = 0.5 + 0.02j$, $0 \le j \le 25$, as well as a suitable set of backward-time isochrons. The inset in each figure shows an enlargement of a region between $\Gamma_{\rm s}$ and $\Gamma_{\rm u}$ to help illustrate some of the detail. Figure 7 is at $c = 2$ before the CIFT bifurcation and also shows 26 backward-time isochrons for $\Gamma_{\rm u}$. Although both isochron foliations $\mathcal{I}(\Gamma_{\rm s})$ and $\mathcal{U}(\Gamma_{\rm u})$ feature regions with high curvature, the two sets of isochrons intersect each other only transversally. Figure 8 is at $c = 2.0071$, which is approximately at the moment of the CIFT bifurcation, and shows 26 corresponding backward-time isochrons of $\Gamma_{\rm u}$, whose phases are chosen such that the isochrons have cubic tangencies with the forward-time isochrons. Figure 9 is at $c = 2.03$, which is after the CIFT bifurcation, and shows the 26 corresponding pairs of backward-time isochrons of $\Gamma_{\rm u}$ that have quadratic tangencies with the forward-time isochrons.

In Fig. 6(a) and (b), the forward-time isochron $I(\gamma_0)$ only has tangencies with certain backward-time isochrons and each tangency is a local feature. However, the point of tangency is transported to other forward-time and backward-time isochrons under the flow. We determine the backward-time isochrons shown in Figs. 7–9, by mapping under the flow in forward and backward time, the intersection point of $I(\gamma_0)$ and the corresponding backward-time isochrons before, at and after the bifurcation that are shown in the left column of Fig. 6. Hence, at the CIFT bifurcation in Fig. 8, the cubic tangency occurs along a single orbit O^* that converges to $\Gamma_{\rm s}$ in forward time and to $\Gamma_{\rm u}$ in backward time. Similarly, there are two orbits O^+ and O^- along which one finds quadratic tangencies after the CIFT bifurcation in Fig. 9; these orbits are shown in green. The selection of backward-time isochrons were chosen such that their tangencies with the forward-time isochrons occur along a portion of O^*, O^+ and O^- that lies near $\Gamma_{\rm s}$. The insets in Figs. 8 and 9 show that other portions of O^*, O^+ and O^- away from $\Gamma_{\rm s}$ are associated with tangencies between different forward-time and backward-time isochrons.

The orbits O^*, O^+ and O^- transport the respective tangency through the annulus bounded by $\Gamma_{\rm s}$ and $\Gamma_{\rm u}$. One can particularly see the tangency between forward-time and backward-time isochrons close to $\Gamma_{\rm s}$, where the forward-time isochrons are relatively straight while the backward-time isochrons have high curvature; compare with the opposite situation in Fig. 6(a2), which is near $\Gamma_{\rm u}$. The CIFT bifurcation can be viewed as a regular

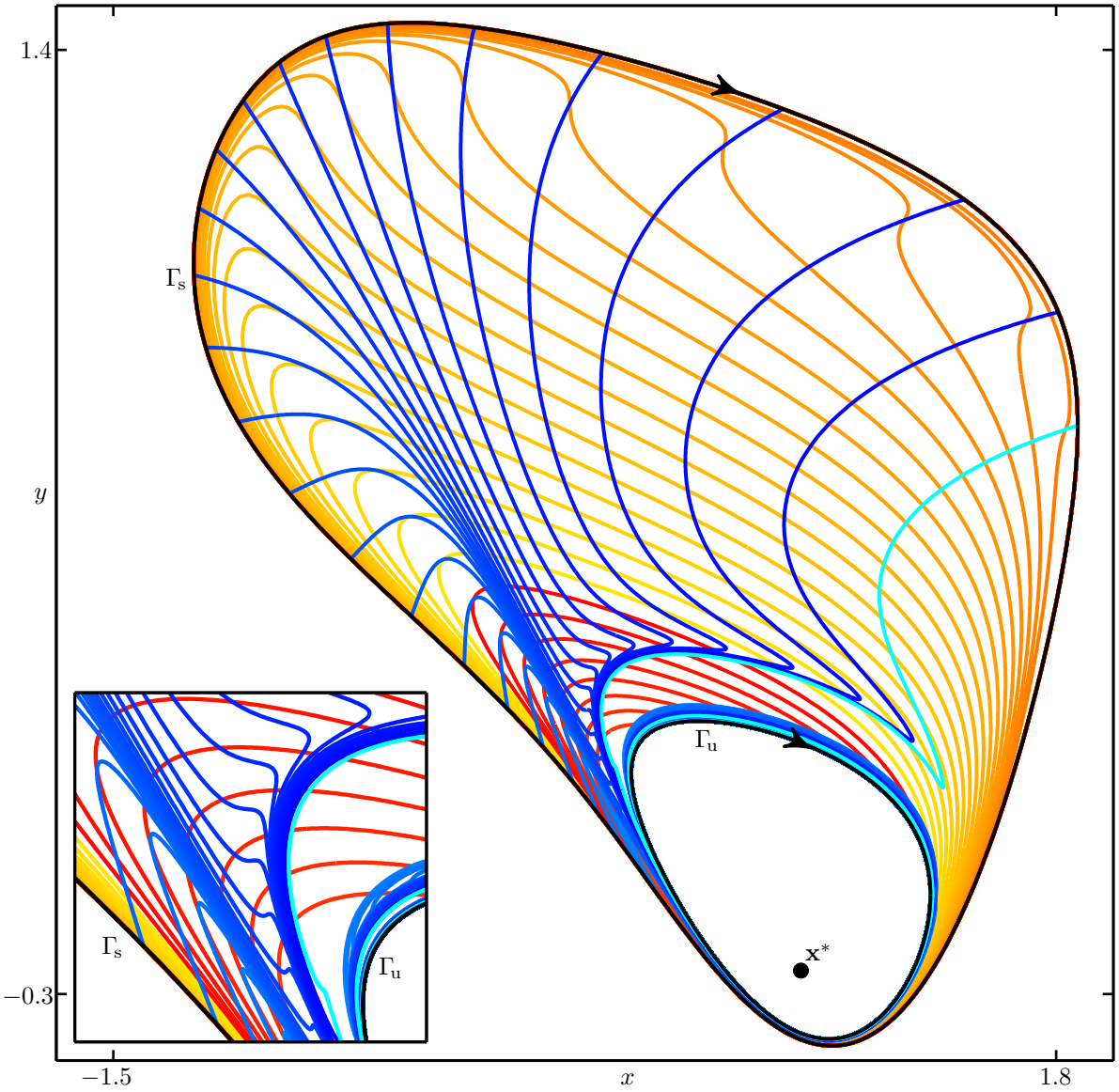

Figure 7: Isochrons of (8) for $c = 2$; shown are 26 forward-time isochrons with phases from 0.5 to 1 in steps of 0.02, which transversally intersect a selection of 26 backward-time isochrons.

fold point where the cubic tangency orbit O^* gives rise to the quadratic tangency orbits $O^{\pm}$.

4.3 Non-transverse isochrons past the Hopf bifurcation

The Hopf bifurcation in the FitzHugh-Nagumo model occurs at $c_{\mathsf{H}} \approx 2.1192$, which is after the occurrence of the CIFT bifurcation at $c \approx 2.0071$. We can continue the backward-time isochron foliations through the Hopf bifurcation as isochrons of the focus equilibrium $\mathbf{x}^*$. Hence, we still expect to observe the corresponding tangencies with the forward-time isochrons.

Figure 10 shows ten forward-time and backward-time isochrons for $c = 2.1$ and $c = 2.2$, that is, before and after the Hopf bifurcation. In each panel, both isochron sets are uniformly distributed in phase. Panel (a) is

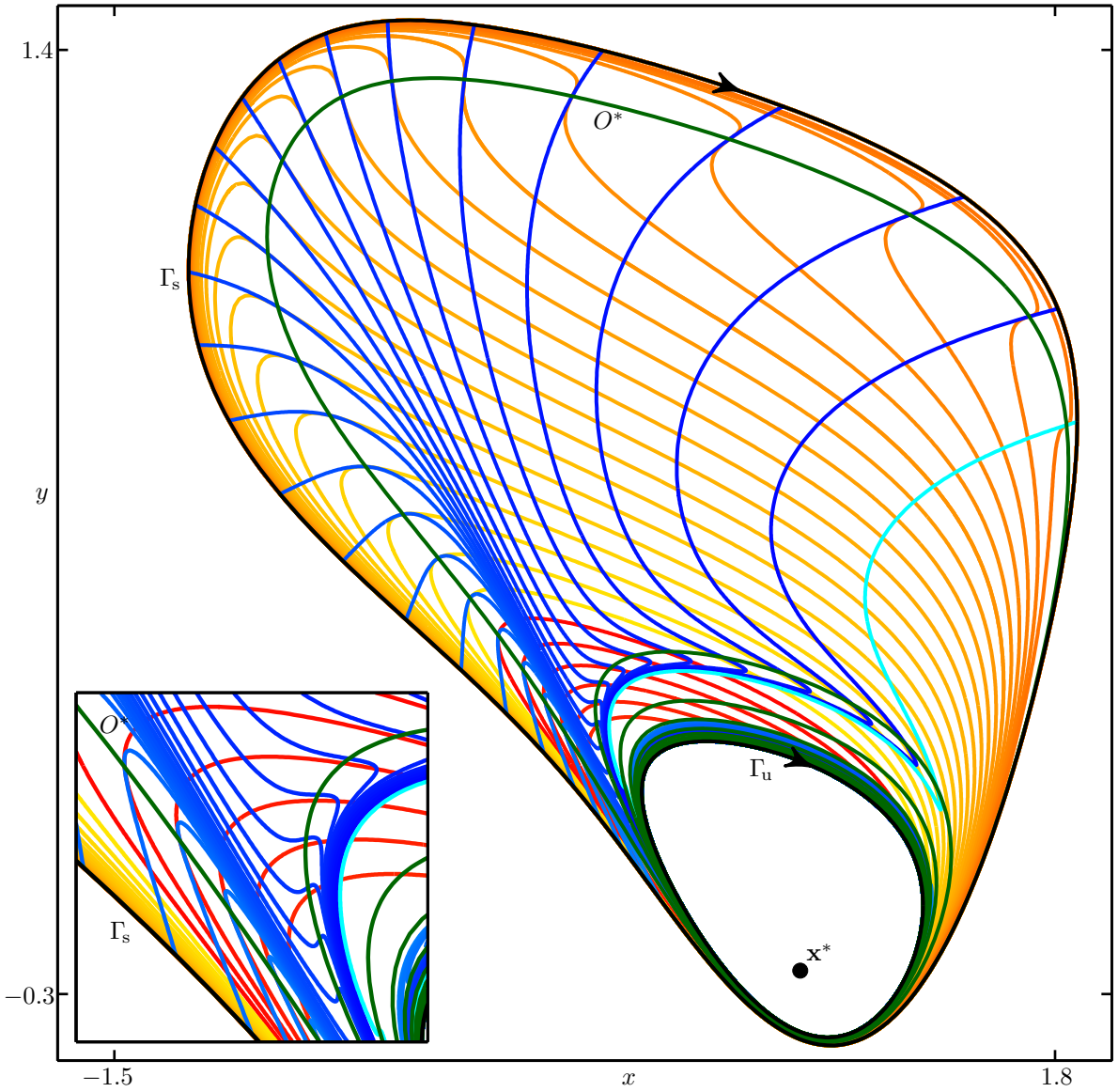

Figure 8: Isochrons of (8) for $c = 2.0071$ approximately at the CIFT bifurcation; shown are 26 forward-time isochrons with phases from 0.5 to 1 in steps of 0.02 that have cubic tangencies with 26 corresponding backward-time isochrons; also shown is the trajectory O^* that passes through the cubic tangencies.

for $c = 2.1$ and shows the backward-time isochrons of the periodic orbit Γ_u with period $T_{\Gamma_u} \approx 6.941$. Panel (b) is for $c = 2.2$ and shows the backward-time isochrons after the Hopf bifurcation for the repelling equilibrium point $\mathbf{x}^*$. The equilibrium point $\mathbf{x}^*$ has eigenvalues $\mu = \alpha \pm \beta i \approx 0.0141 \pm 0.926i$, which gives a natural period of $T_{\mathbf{x}^*} \approx 6.786$.

The selection of ten isochrons $I(\gamma^s_\theta)$ and $U(\gamma^u_\theta)$ with $\theta \in \{0, 0.1, ..., 0.9\}$ makes it harder to see that both panels show a situation past the CIFT bifurcation. However, we clearly see pairs of intersections between two particular backward-time and forward-time isochrons. Similarly, observe in both panels that $I(\gamma^s_{0.9})$ (which exits the image along the top) is almost tangent to $U(\gamma^u_{0.2})$ (just to the right of $I(\gamma^s_{0.9})$ near the top).

The isochrons of Γ_u before the Hopf bifurcation and of $\mathbf{x}^*$ after the Hopf bifurcation are well defined, and

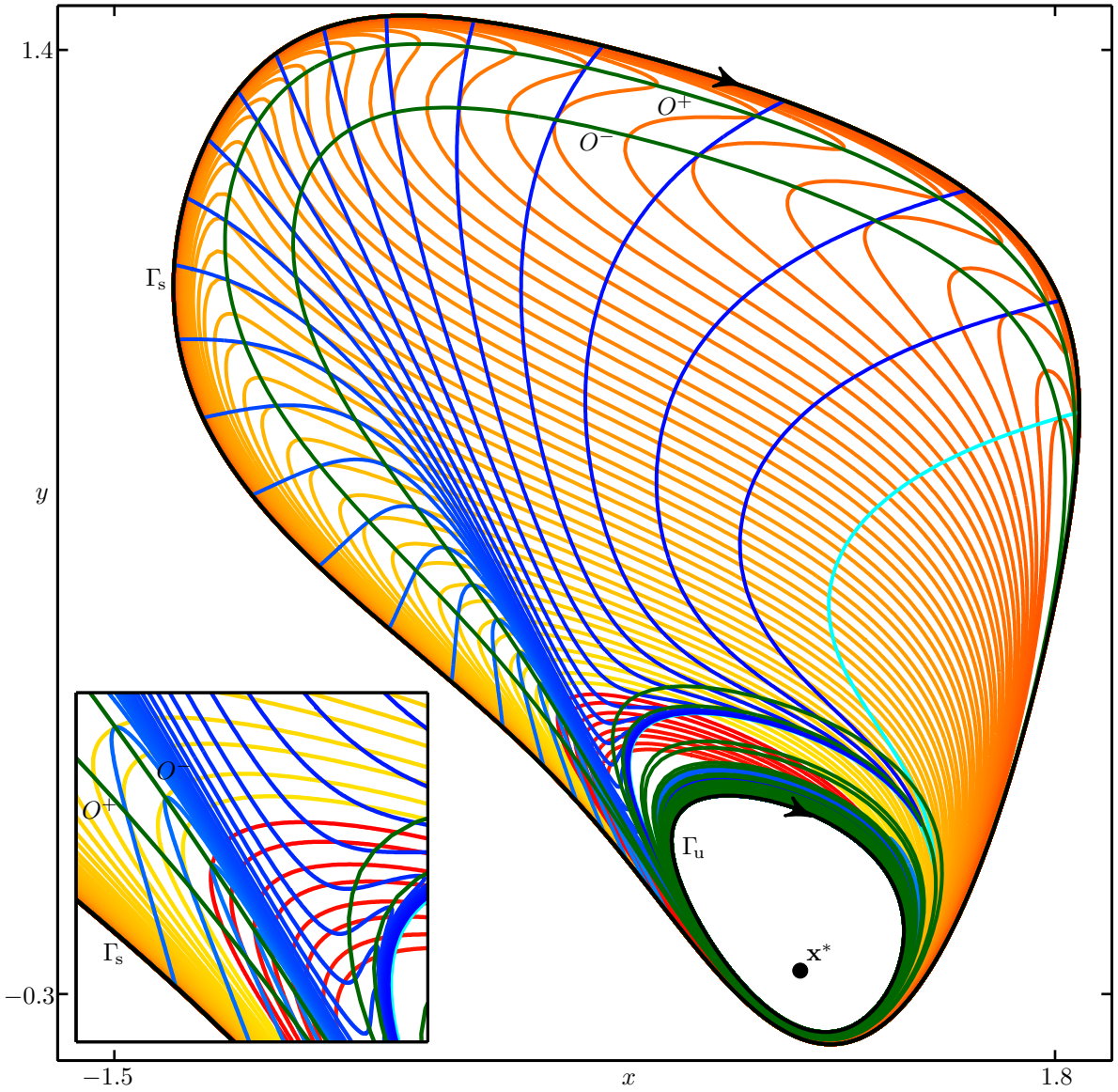

Figure 9: Isochrons of (8) for $c = 2.03$; shown are 26 forward-time isochrons with phases from 0.5 to 1 in steps of 0.02 that have quadratic tangencies with 52 corresponding backward-time isochrons. Also shown are the trajectories O^+ and O^- that pass through respective tangencies.

a comparison of the two panels in Fig. 10 suggests that both isochron foliations, $\mathcal{U}(\Gamma_u)$ and $\mathcal{U}(\mathbf{x}^*)$, converge to the same limit at $c = c_H$. This is evidence that we can, indeed, follow an isochron foliation through a Hopf bifurcation and that our definition of a backward-time isochron foliation of a focus equilibrium is compatible with that of an associated repelling periodic orbit.

Note that, at the Hopf bifurcation, the equilibrium $\mathbf{x}^*_H$ is non-hyperbolic (its eigenvalues $\mu \approx \pm 0.9260i$, are purely imaginary). However, there is a non-zero rotation and its natural period is $T_{\mathbf{x}^*_H} \approx 6.785$ well defined. As stated in Lemma 1 from [24], there is a well-defined foliation of equilibrium isochrons $\mathcal{U}(\mathbf{x}^*_H)$ of $\mathbf{x}^*_H$ at $c = c_H$ that are invariant under the flow for the time-$T_{\mathbf{x}^*_H}$ map; compare with the isochrons of the non-hyperbolic equilibrium in system (7) for $a = 0$ in Section 3.

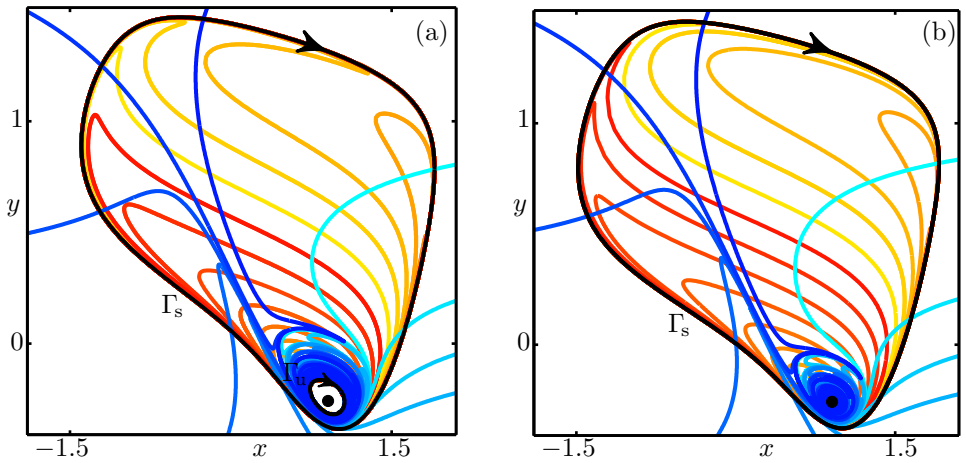

Figure 10: Illustration of isochrons of (8) through a Hopf bifurcation. Panel (a) shows ten isochrons of Γ_s and of Γ_u for $c = 2.1$ before the Hopf bifurcation, and panel (b) shows ten isochrons of Γ_s and of $\mathbf{x}^*$ for $c = 2.2$ after the Hopf bifurcation.

With well-defined isochrons before, at and after the Hopf bifurcation, we conjecture that, for each phase θ, there exists a C^1-smooth c-dependent family that continues the isochron with phase θ through a Hopf bifurcation.

4.4 Non-transverse isochrons for larger time-scale separations

Figure 11 shows isochrons for $c = 2.5$ that is, well past the CIFT bifurcation and the subsequent Hopf bifurcation. We show again the same 26 forward-time isochrons of Γ_s as in Figs. 7–9, and 26 pairs of backward-time isochrons of $\mathbf{x}^*$ that form quadratic tangencies with the forward-time isochrons; note that $\mathbf{x}^*$ is repelling, and has a natural period $T_u \approx 6.801$. Also shown are the two trajectories O^+ and O^- (green curves) that pass through these tangencies. Figure 11 shows a typical relaxation oscillation, which actually has non-transverse isochron intersections. We have also computed backward-time isochrons of the relaxation oscillation in the reduced Hodgkin-Huxley model studied in [23], and found that it also features tangencies between forward-time and backward-time isochrons. These examples provide strong numerical evidence for the conjecture that a relaxation oscillation in a planar system with a cubic nullcline has non-transverse forward-time and backward-time foliations, provided the time-scale separation parameter is sufficiently small.

5 Model equations with CIFT bifurcation

In this section we are interested in what mechanisms lead to a CIFT bifurcation. In the FitzHugh-Nagumo system, it is due to a variation in the time-scale separation parameter c. We isolate this property by first constructing a simple model that has only transverse isochron foliations, and introduce a time-scale separation parameter that globally scales one variable. This provides more control of this property than in the FitzHugh-Nagumo system and, indeed, we show in Section 5.1 that, if the time-scale separation is sufficiently large, a CIFT bifurcation occurs.

In Section 5.2, we show that only a local perturbation to the dynamics is required for creating a CIFT bifurcation. In the same spirit as Section 5.1, we start with a simple model that exhibits only transverse isochron foliations and, by perturbing a small region of the vector field via a bump function, we can create a CIFT bifurcation when the magnitude of the bump function is large enough. Importantly, the trajectory curves in the phase plane remain unchanged in this construction.

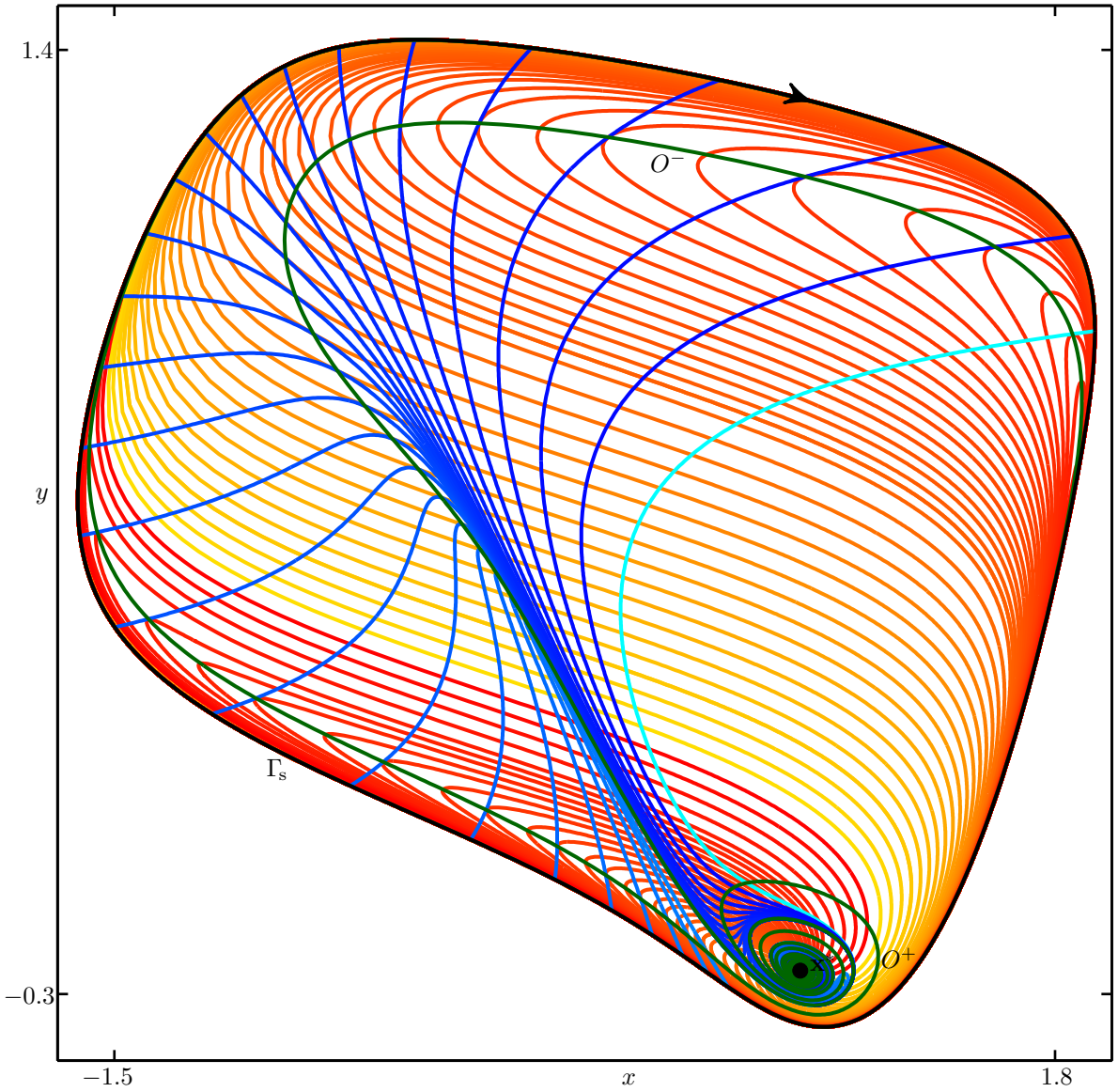

Figure 11: Isochrons for $c = 2.5$. Shown are 26 forward-time isochrons with phases from 0.5 to 1 in steps of 0.02, and a selection of backward-time isochrons that have quadratic tangencies with them; also shown are the trajectories O^+ and O^- that pass through the respective tangencies.

In Section 5.3, we show the isochrons associated with a relaxation oscillation arising from a canard explosion in the Van der Pol system, which is another example of a relaxation oscillation with a cubic nullcline. We show, firstly, that the relaxation oscillation exhibits non-transverse isochron foliations, which supports the conjecture from Section 4.4 and, secondly, that the canard explosion is a mechanism for creating the CIFT bifurcation.

5.1 Global time-scale separation

In this section we demonstrate that a sufficiently large global time-scale separation creates a CIFT bifurcation. Specifically we present a simple model with transverse isochron foliations and then introduce a time-scale

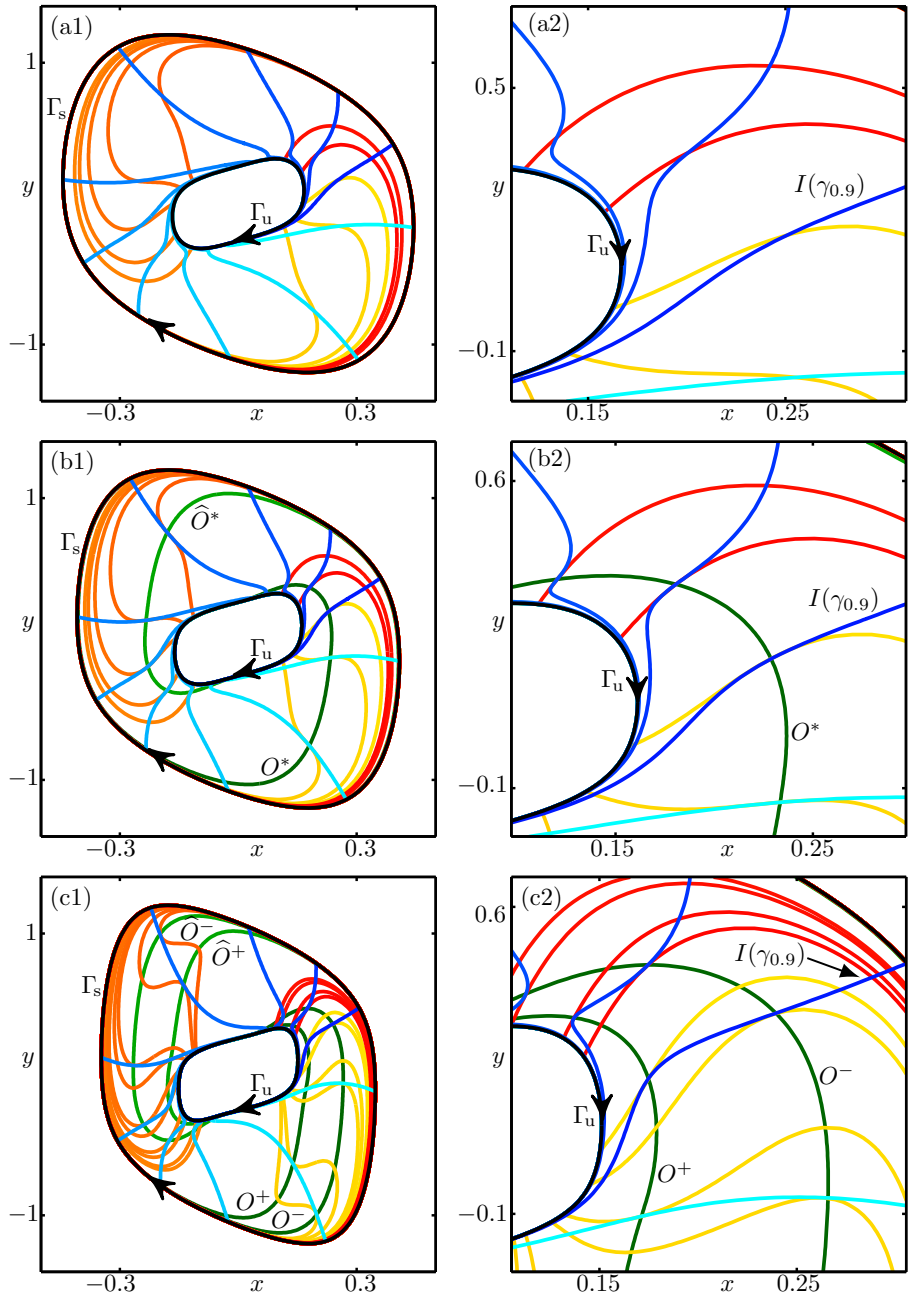

Figure 12: Shown is a CIFT bifurcation that occurs between forward-time and backward-time isochrons in system (9). Row (1) shows the phase portrait for $\varepsilon = 0.1$, where no tangencies occur between the two sets of isochrons. Row (2) shows the phase portrait for $\varepsilon = 0.08$, where each forward-time isochron locally forms a cubic tangency with a particular backward-time isochron; the trajectory O^* passes through all of the cubic tangencies. Row (c) shows the phase portrait for $\varepsilon = 0.05$, where each forward-time isochron locally forms a quadratic tangency with two backward-time isochrons; the trajectories O^+ and O^- pass through each of the tangencies.

separation parameter. Namely, we consider the model given in polar coordinates by

$$\begin{cases} \dot{r} &= -(r-1)(r-a), \\ \dot{\psi} &= -\left(\omega\,\frac{r-1}{a-1} + 1 - \frac{r-1}{a-1}\right), \end{cases}$$

where we fix the parameters $a = 0.25$, $\omega = 0.5$. The model (5.1) is qualitatively the simple model (7) introduced by Winfree, and the isochrons can be calculated explicitly. There is an attracting periodic orbit $\Gamma_{\rm s}$, which is the unit circle, a repelling periodic orbit $\Gamma_{\rm u}$ at $r = a$, and the family of trajectories of system (5.1) is invariant under any translation of ψ (mod 2π). The flow on both periodic orbits is clockwise, where the angular velocity on $\Gamma_{\rm s}$ is constant at $\dot{\psi} = -1$ and on $\Gamma_{\rm u}$ it is constant at $\dot{\psi} = -\omega$. Since we set $\omega = 0.5$, the rotation on $\Gamma_{\rm s}$ is faster than on $\Gamma_{\rm u}$, with $T_{\rm s} = 2\pi$ and $T_{\rm u} = 4\pi$. Here, we are only interested in the forward-time isochrons $\mathcal{I}(\Gamma_{\rm s})$ and the backward-time isochrons $\mathcal{U}(\Gamma_{\rm u})$ of the periodic orbits $\Gamma_{\rm s}$ and $\Gamma_{\rm u}$, respectively, and consider the annulus where the two foliations coexist. The angular velocity in the region $a < r < 1$ between $\Gamma_{\rm s}$ and $\Gamma_{\rm u}$ varies linearly with r.

We write system (5.1) in Cartesian coordinates, and introduce a time-scale separation between the x- and y-variables given by the parameter $0 < \varepsilon \ll 1$, which yields:

$$\begin{cases} \dot{x} &= \varepsilon\left(\left(1-\sqrt{x^2+y^2}\right)\left[x\left(\frac{\sqrt{x^2+y^2}-a}{\sqrt{x^2+y^2}}\right) - y\left(\frac{\omega-1}{a-1}\right)\right] + y\right), \\ \dot{y} &= \left(1-\sqrt{x^2+y^2}\right)\left[y\left(\frac{\sqrt{x^2+y^2}-a}{\sqrt{x^2+y^2}}\right) + x\left(\frac{\omega-1}{a-1}\right)\right] - x. \end{cases} \tag{9}$$

When the time-scale separation parameter $\varepsilon = 1$, system (9) has the properties discussed above. As soon as $\varepsilon < 1$, system (9) only has the symmetry generated by the map $(x, y) \mapsto (-x, -y)$. The periodic orbits $\Gamma_{\rm s}$ and $\Gamma_{\rm u}$ persist and remain nested; the flow on each periodic orbit is still clockwise, but the rotation is no longer constant and the period changes. We are interested in the intersections of $\mathcal{I}(\Gamma_{\rm s})$ and $\mathcal{U}(\Gamma_{\rm u})$ in the region between $\Gamma_{\rm s}$ and $\Gamma_{\rm u}$ as we decrease ε.

Figure 12 illustrates the isochrons in the region bounded by $\Gamma_{\rm s}$ and $\Gamma_{\rm u}$ for three values of ε, namely, $\varepsilon = 0.1$ before, $\varepsilon = 0.08$ approximately at, and $\varepsilon = 0.05$ after the CIFT bifurcation. The left column shows the entire region, and the right column shows an enlargement of some isochron intersections. In each panel, we computed ten forward-time isochrons uniformly distributed in phase, and a selection of backward-time isochrons. The panels of Fig. 12 show that the forward-time isochrons accumulate on $\Gamma_{\rm u}$ clockwise because the period $T_{\rm u}$ is larger than $T_{\rm s}$, that is, $\Gamma_{\rm u}$ rotates with a slower speed than $\Gamma_{\rm s}$. For this reason the backward-time isochrons also accumulate on $\Gamma_{\rm s}$ clockwise.

Figure 12(a) shows the situation for $\varepsilon = 0.1$. At this parameter value, $T_{\rm s} \approx 24.626$, and $T_{\rm u} \approx 54.296$. This figure illustrates the situation before the CIFT bifurcation, where $\mathcal{I}(\Gamma_{\rm s})$ is transverse to $\mathcal{U}(\Gamma_{\rm u})$. For example, consider the dark-blue isochron $I(\gamma_{0.9})$, which is almost a straight line before it begins to spiral around $\Gamma_{\rm u}$. Panel (a2) shows how $I(\gamma_{0.9})$ crosses three backward-time isochrons of $\mathcal{U}(\Gamma_{\rm u})$ transversally; compare also panel (a1).

Figure 12(b) for $\varepsilon = 0.08$ illustrates the moment of the CIFT bifurcation: approximately at this parameter value cubic tangencies appear. Here, $T_{\rm s} \approx 28.426$ and $T_{\rm u} \approx 64.799$. We show ten corresponding backward-time isochrons that have cubic tangencies with the forward-time isochrons shown. We also show in green the trajectory O^* and its symmetric copy, denoted $\widehat{O}^*$, along which cubic tangencies occur. At the point at which a forward-time isochron intersects O^* or $\widehat{O}^*$, it has a cubic tangency with a backward-time isochron. For example, the forward-time isochron $I(\gamma_{0.9})$ is still transverse to most of the backward-time isochrons in Fig. 12(b), but the enlargement in panel (b2) shows that it has a cubic tangency as it crosses O^*.

Figure 12(c) shows the phase plane for $\varepsilon = 0.05$, after the CIFT bifurcation. Here, $T_{\rm s} \approx 38.635$ and $T_{\rm u} \approx 95.542$. For each of the ten forward-time isochrons in row (b), we computed a corresponding pair of backward-time isochrons that have quadratic tangencies with the forward-time isochrons. We also show the symmetrically related pairs of trajectories $O^{\pm}$ and $\widehat{O}^{\pm}$, along which we find quadratic tangencies.

Observe how $I(\gamma_{0.9})$ now curves anti-clockwise after it crosses O^-, until it intersects O^+, where it curves clockwise again. This behavior can be observed for all forward-time isochrons. Similarly, the backward-time

isochrons curve clockwise, as they cross O^+ ($\widehat{O}^+$), and back as they approach O^- ($\widehat{O}^-$); see the bottom right or (symmetric) top left region of the annulus in Fig. 12(c1).

As in Section 4, regions of varying dynamics play a role in the formation of the isochron geometry. The higher curvature of $I(\gamma_{0.9})$ and other forward-time isochrons near O^+ means that trajectories starting close to O^+ are some of the fastest trajectories in the system. Similarly, initial points near O^- correspond to some of the slowest trajectories in the system.

This example provides a distilled version of what happens in the FitzHugh-Nagumo model where the parameter c creates a CIFT bifurcation. It shows that scaling a system globally with a time-scale separation in this way provides a mechanism for creating a CIFT bifurcation.

5.2 Local generation of a CIFT bifurcation

In this section, we show that a CIFT bifurcation can be created by a local perturbation of a system with transverse isochron foliations. Indeed, any locally created cubic tangency is mapped forward and backward in time under the flow throughout the respective basins so that the tangency actually has a global effect. Moreover, we apply the local perturbation only to the time parameterization, which means that the actual trajectories are unchanged as curves in the phase plane and the periods of $\Gamma_{\rm s}$ and $\Gamma_{\rm u}$ also remain unchanged.

We consider again the simple model (7) that was introduced by Winfree [29], with $a = 0.25$ and $\omega = -0.5$. Recall that $\Gamma_{\rm s}$ is the unit circle, which is attracting and has period $T_{\rm s} = 2\pi$, and inside $\Gamma_{\rm s}$ there is a repelling periodic orbit $\Gamma_{\rm u}$, which is the circle $r = 0.25$, and has period $T_{\rm u} = 3.2\pi$. The system is rotationally symmetric under any rotation about the origin, and the forward-time and backward-time isochrons are spiraling curves that are also symmetric under any rotation.

We now introduce a perturbation as a time parameterization, which scales both the x- and y-variables equally, in a small domain Ω of the annulus between $\Gamma_{\rm s}$ and $\Gamma_{\rm u}$. More specifically, we let Ω be the angular sector with $r \in [0.725, 0.775]$ and $\psi \in [-\frac{\pi}{24}, \frac{\pi}{24}]$. We define a bump function $g(x, y; \kappa)$ with $g \equiv 1$ outside Ω that depends on a parameter κ inside Ω. We require that g has maximum κ at the midpoint in Ω and equals 1 along the boundary of Ω. To this end, we construct a 12th-degree polynomial in one variable over the interval $[-1, 1]$, which has maximum 1 and is 0 at the boundary. We apply this polynomial to the radial direction r and to the angular direction ψ, rescaled to the corresponding r- or ψ-interval, as defined above. We write $g(x, y; \kappa)$ in Cartesian coordinates, and define it to be 1 outside of Ω, and 1 plus κ times the value of the polynomial bump function in r and ψ. We could construct the bump function $g(x, y; \kappa)$ such that it is C^∞-smooth on the boundary of Ω; however, C^3-differentiability is sufficient for our purposes; the precise definition of $g(x, y; \kappa)$ is given in the Appendix. We now modify (7) as follows:

$$\begin{cases} \dot{x} &= g(x, y; \kappa) f_1(x, y), \\ \dot{y} &= g(x, y; \kappa) f_2(x, y). \end{cases} \tag{10}$$

We consider the parameter range $\kappa \geq 1$, such that $g(x, y; \kappa)$ has the effect of a local acceleration. Since, $g(x, y; \kappa)$ only alters the time parameterization of trajectories, the trajectory curves in the phase plane are still symmetric under rotation, but the underlying dynamics is not. As a consequence, the forward-time and backward-time isochrons change with κ and are no longer symmetric.

Figure 13 shows forward-time and backward-time isochron foliations before, at and after the CIFT bifurcation for system (10) at $\kappa = 0.25$, $\kappa = 1.3$, and $\kappa = 50$, respectively. The left column shows the annulus bounded by $\Gamma_{\rm s}$ and $\Gamma_{\rm u}$ with ten forward-time isochrons of $\Gamma_{\rm s}$, which are uniformly distributed in phase, and selected backward-time isochrons of $\Gamma_{\rm u}$. The right column shows an enlargement near Ω. In each panel, the sector Ω is outlined and the greyscale in the interior of Ω indicates the magnitude of κ, that is, the magnitude of the local acceleration applied to the flow.

Figure 13(a) is at $\kappa = 0.25$, for which we plot sixteen backward-time isochrons. Panel (a1) illustrates that all intersections are still transverse, even though the isochrons are no longer perfect spirals; this can particularly be observed in the forward-time isochrons, e.g., in the top-right corner of panel (a2). Figure 13(b) shows the situation for $\kappa = 1.3$, which is the approximate parameter value of the CIFT bifurcation, where the forward-time isochrons form cubic tangencies with sixteen backward-time isochrons. Note how the trajectory O^* that

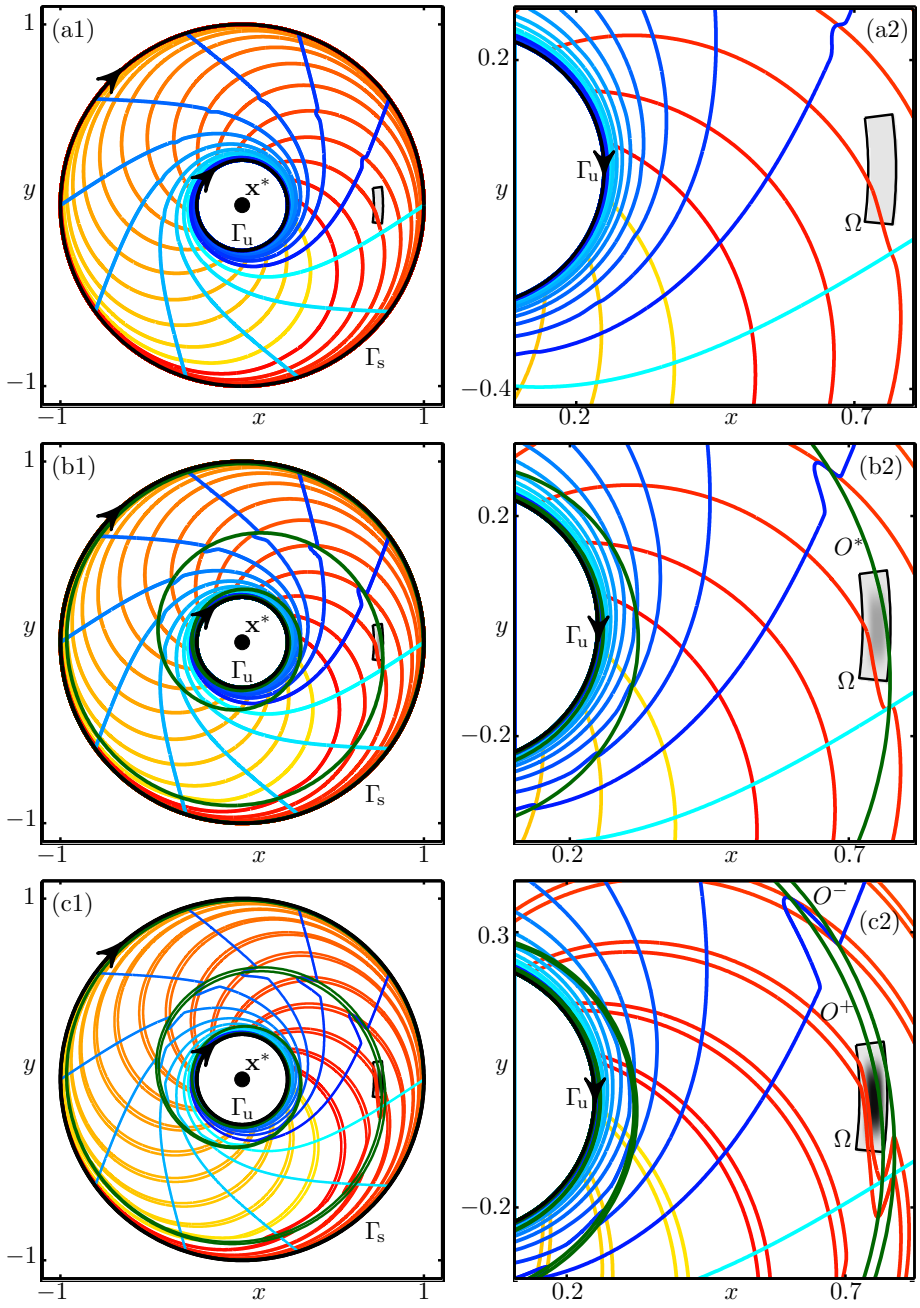

Figure 13: The CIFT bifurcation for system (10); compare with Fig. 12. The sector outlined in black is the region where the flow velocity is increased; its magnitude is determined by the greyscale within the box Ω.

passes through each cubic tangency remains a perfect spiral even though it passes through Ω. Figure 13(c) shows the case for $\kappa = 50$. Here non-transverse intersections occur by way of quadratic tangencies between each forward-time isochron and sixteen pairs of backward-time isochrons. These tangencies occur along the two trajectories O^+ and O^-, which are again perfect spirals even though they both pass through Ω.

In this example, the curved geometry of the isochrons that give rise to tangencies are created solely due to the acceleration along trajectories that pass through Ω. Although not all isochrons pass through Ω, the

trajectories that do pass through it intersect all isochrons. Therefore, the influence of the perturbation is felt throughout both sets of isochrons in the annulus as given by the trajectories O^*, O^+ and O^-.

Since the ratio between the periods of Γ_s and Γ_u is rational, each forward-time isochron has tangencies with a finite set of backward-time isochrons. If the forward-time isochron $I(\gamma^s)$ is tangent to the backward-time isochron $U(\gamma^u)$, then $I(\gamma^s)$ has infinitely many tangencies with only 8 backward-time isochrons, namely, $\{U(\gamma^u_\vartheta) \mid \vartheta = \theta_u(\gamma^u) + \frac{5}{8}m \pmod 1, m \in \mathbb{N}\}$. Similarly, $U(\gamma^u)$ has infinitely many tangencies with only 5 forward-time isochrons separated by the phase difference $\frac{2\pi}{5}$.

This example shows that increasing the amplitude of the bump function in the sector Ω is indeed a sufficient mechanism to create non-transverse isochron foliations. Furthermore, since we only rescale time, the phase curves remain unchanged in the (x, y)-plane as we vary the magnitude of the bump function. Hence, the vector fields before and after the CIFT bifurcation in system (10) provide an example of two vector fields that are orbitally topologically equivalent, but are not conjugate.

Our construction of the local perturbation in this example uses a C^3-smooth polynomial bump function on a sector domain made up of angular and radial intervals; however, we conjecture that the construction is entirely general. Given any planar vector field with an annulus where both forward-time and backward-time isochron foliations coexist, then a rescaling of time in a small domain in the annulus will cause non-transverse forward-time and backward-time foliations for the vector field, provided the magnitude of the time rescaling is sufficiently large; the required magnitude will depend on the area of the domain in which the rescaling is applied.

5.3 CIFT bifurcation in a canard explosion

A canard explosion is a rapid transition from a periodic orbit born in a Hopf bifurcation to a relaxation oscillation that exhibits clear epochs of fast and slow dynamics. During this transition, which occurs in an exponentially small parameter interval, there is a rapid growth in the amplitude of the periodic orbit while it follows the repelling slow manifold of the system before jumping to attracting branches [4, 5]. In this section we show that a canard explosion is also a mechanism for creating a CIFT bifurcation.

We present this mechanism with the example of the canard explosion in the planar Van der Pol system [27]; this example also demonstrates how one can observe a CIFT bifurcation between isochrons of a periodic orbit and a focus equilibrium. The Van der Pol system is the planar slow-fast system given by

$$\begin{cases} \varepsilon\dot{x} &= y - \frac{1}{3}x^3 + x, \\ \dot{y} &= \lambda - x. \end{cases} \tag{11}$$

For $\varepsilon \ll 1$, system (11) has a time-scale separation, where x is fast and y is slow; the x-nullcline is given by the cubic curve

$$y = \frac{1}{3}x^3 - x, \tag{12}$$

and the y-nullcline is given by the line

$$x = \lambda.$$

Hence, system (11) has an equilibrium $\mathbf{x}^* =: (x, y) = (\lambda, \frac{1}{3}\lambda^3 - \lambda)$, which is stable for $|\lambda| > 1$ and unstable for $|\lambda| < 1$. At $\lambda = \pm 1$, supercritical Hopf bifurcations occur. Here, we are interested in the interaction between forward-time and backward-time isochrons near the bifurcation for $\lambda = \lambda_H = 1$.

Theory predicts that the periodic orbit born in the Hopf bifurcation is initially small. Generically, the period of the periodic orbit and the natural period of the equilibrium move away from each other with a non-zero speed as the periodic orbit grows in amplitude when λ decreases away from the Hopf bifurcation point. Hence, each set of isochrons spiral to their respective accumulation limits, and the two sets spiral in opposite directions. In particular, close to the Hopf bifurcation, this means that the two isochrons foliations intersect transversally. On the other hand, system (11) exhibits relaxation oscillations. These are typically attributed to trajectories following the slow branches of the critical manifold separated by fast jumps. The x-nullcline given by (12) is the critical manifold of system (11). The maximum and minimum of the cubic curve at $x = \pm 1$ separate the critical manifold into three branches, where the left and right branches are attracting, and the middle branch is repelling.

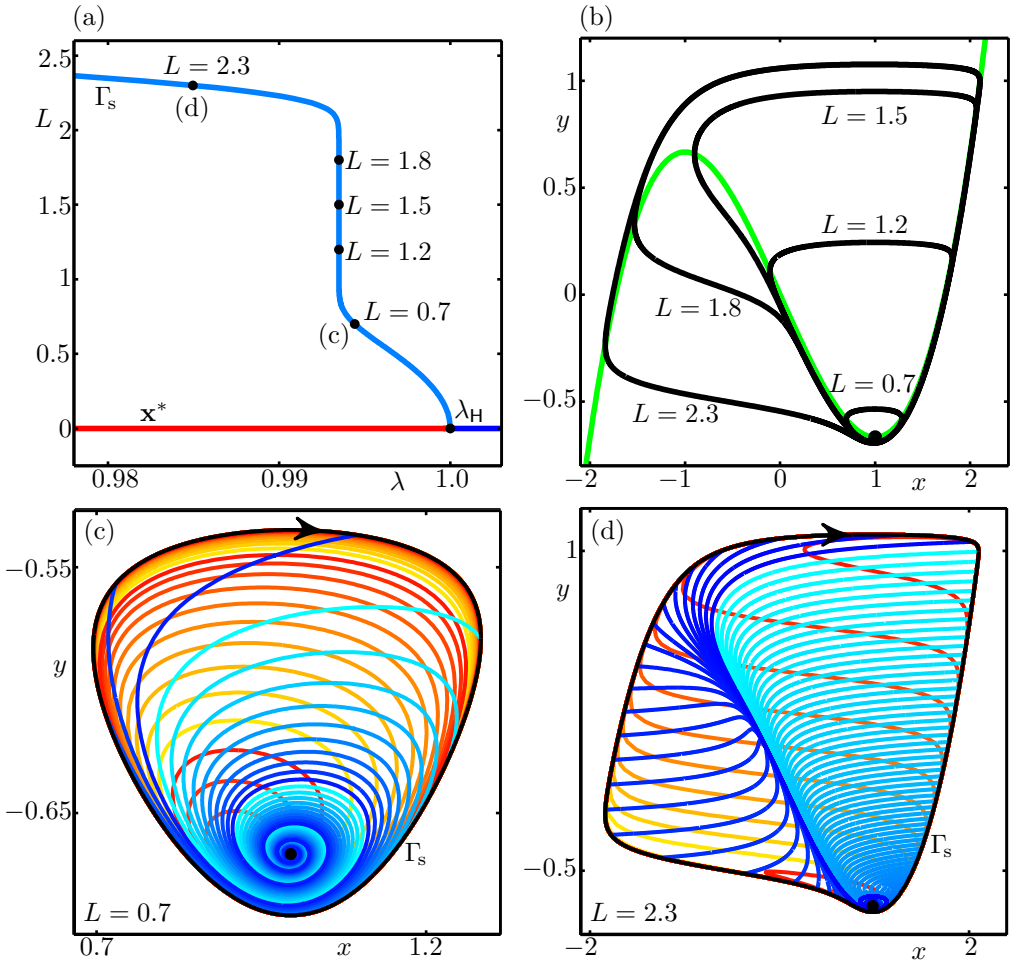

Figure 14: Canard explosion of the Van der Pol system (11) with $\varepsilon = 0.05$. Panel (a) shows a one-parameter bifurcation diagram in the (λ, L)-plane, where L is the arclength of the solutions. Shown is the equilibrium $\mathbf{x}^*$, (stable when blue, unstable when red) and attracting periodic orbit Γ_s that emanates from a Hopf bifurcation at $\lambda_H = 1$. The five labelled points correspond to the periodic orbits Γ_s when it has arclengths $L = \{0.7, 1.2, 1.5, 1.8, 2.3\}$, which is shown in panel (b) together with the critical manifold (green), and the equilibrium $\mathbf{x}^* = (1, -\frac{2}{3})$ at $\lambda = \lambda_H$ (black dot). Panel (c) shows ten forward-time isochrons of Γ_s with $L = 0.7$ and ten backward-time isochrons of $\mathbf{x}^*$. Panel (d) shows one hundred forward-time isochrons of Γ_s with $L = 2.3$ and ten backward-time isochrons of $\mathbf{x}^*$.

When $\varepsilon > 0$ is sufficiently small, a trajectory slowly follows each attracting branch of the critical manifold order $O(\varepsilon)$ close, until it reaches an extremum where there is a fast jump to the other attracting branch, creating the typical relaxation oscillation of the Van der Pol system. Such relaxation oscillations typically exhibit large time-scale separations; hence, we expect the isochron foliations of a relaxation oscillation in system (11) and of its equilibrium to have non-transverse intersections.

Figure 14 illustrates the canard explosion near λ_H and associated isochron foliations. Figure 14(a) shows a one-parameter bifurcation diagram in the (λ, L)-plane of (11) for $\varepsilon = 0.05$, where L is the arclength of the solution. The line $L = 0$ represents $\mathbf{x}^*$. A curve representing attracting periodic orbits Γ_s emanates from λ_H, which undergoes a canard explosion as λ decreases from λ_H. Close to the Hopf bifurcation, the arclength of the periodic orbits grows like $\sqrt{\lambda_H - \lambda}$ [15]. This is then followed by a steep segment at $\lambda \approx 0.9935$, which

signifies a rapid increase in arclength, before a plateau of the arclength L of the periodic orbits is reached. The points labelled in Fig. 14(a) correspond to periodic orbits with arclengths $L \in \{0.7, 1.2, 1.5, 1.8, 2.3\}$. The three intermediate periodic orbits are examples of canard orbits and their λ-values only vary in the eighth decimal place; however, with numerical continuation the periodic orbits of this family can be found reliably and distinguished by arclength. The periodic orbits with $L = 0.7$ and $L = 2.3$ are at $\lambda \approx 0.9944$ and $\lambda \approx 0.9850$, respectively.

Figure 14(b) shows the periodic orbit Γ_s in the (x, y)-plane for the five different values of the arclength L as labelled in panel (a), together with the critical manifold (green) and also the equilibrium $\mathbf{x}^*$ at the moment of Hopf bifurcation at $\lambda_H = 1$. Observe that all three canard orbits track a significant part of the repelling branch of the critical manifold before making a fast jump to an attracting branch. The small periodic orbit with $L = 0.7$ lies close to the equilibrium and only briefly follows the repelling critical manifold. The periodic orbit with $L = 1.2$ follows the repelling slow manifold for longer before making a fast jump to the right attracting branch. The periodic orbit with $L = 1.5$ is known as the maximal canard, as it follows the repelling branch for the longest time before making a fast jump to the right attracting branch of the critical manifold. Finally, the periodic orbit with $L = 1.8$ again follows the repelling branch, but not quite as far, and then jumps to the left attracting branch. The periodic orbit with $L = 2.3$ is a typical example of a relaxation oscillation: it almost immediately jumps to the left attracting branch, which it follows until just after the maximum, where it makes a fast jump to the right attracting branch, before closing up on itself.

Figure 14(c) shows the interaction between forward-time and backward-time isochrons before the rapid increase in arclength of the canard explosion, when the attracting periodic orbit Γ_s has arclength $L = 0.7$. Shown are ten forward-time isochrons of Γ_s and ten backward-time isochrons of the repelling equilibrium $\mathbf{x}^*$. The forward-time isochrons accumulate on $\mathbf{x}^*$ and the backward-time isochrons accumulate on Γ_s. Both sets of isochrons are uniformly distributed in phase; here, $T_s \approx 1.8078$ and $T_u \approx 0.6666$. The foliations of forward-time and backward-time isochrons intersect each other only transversally, and the situation is topologically equivalent to that in Fig. 3(c2).

Figure 14(d) shows $\mathcal{I}(\Gamma_s)$ and $\mathcal{U}(\mathbf{x}^*)$ when Γ_s has arclength $L = 2.5$. We plot one hundred forward-time isochrons of Γ_s and ten backward-time isochrons of $\mathbf{x}^*$, which are both uniformly distributed in phase; here, $T_s \approx 3.8392$ and $T_u \approx 0.9876$. The foliations $\mathcal{I}(\Gamma_s)$ and $\mathcal{U}(\mathbf{x}^*)$ are no longer transverse for this case. This can be seen, for example, in the middle of Fig. 14(d) near the bottom part of Γ_s, where the backward-time isochron $U(\gamma_{0.9})$ is almost tangent to one of the hundred forward-time isochrons shown from $\mathcal{I}(\Gamma_s)$.

Figures 14(c) and (d) illustrate that a CIFT bifurcation occurs at some point during the canard explosion. During the canard explosion, Γ_s grows very fast with λ, and the isochrons are very sensitive, which makes it difficult to compute them for small ε. Hence, in order to visualize isochrons in the canard explosion and identify the actual moment of the CIFT bifurcation, we consider a larger time scale separation parameter, namely, $\varepsilon = 0.2$. For this parameter value the two distinct time scales are less pronounced, but as shown in Figs. 15 and 16, a CIFT bifurcation still occurs and we are able to visualize it.

Figure 15(a) shows the bifurcation diagram in the (λ, L)-plane for (11) with $\varepsilon = 0.2$. It is qualitatively as Fig. 14(a) and shows $\mathbf{x}^*$ as a line at $L = 0$ and Γ_s as a branch of attracting periodic orbits emanating from the Hopf bifurcation at $\lambda_H = 1$. Here, the steep segment of the branch of periodic orbits is less pronounced than in Fig. 14(a), due to the weaker time-scale separation. Nevertheless, close to λ_H, the periodic orbit Γ_s grows as $\sqrt{\lambda_H - \lambda}$, which is followed by a clear region of more rapid growth in arclength. The four labelled points correspond to arclengths of Γ_s for $L = 0.4$ ($\lambda \approx 0.9931$), $L = 1.2$ ($\lambda \approx 0.9690$), $L_{CIFT} \approx 1.7842$ ($\lambda \approx 0.9434$) and $L = 2$ ($\lambda \approx 0.8943$). Panel (b) shows Γ_s at the corresponding points in the (x, y)-plane, and also the equilibrium $\mathbf{x}^*$ at the Hopf bifurcation.

Figure 16 shows the associated forward-time isochrons for each of the four periodic orbits Γ_s, and backward-time isochrons of $\mathbf{x}^*$. In each case, ten forward-time isochrons are shown, which are uniformly distributed in phase, and also a selection of backward-time isochrons of $\mathbf{x}^*$. Panel (a) shows forward-time isochrons of the periodic orbit Γ_s with arclength $L = 0.4$, which is near the Hopf bifurcation. Also shown are ten backward-time isochrons of $\mathbf{x}^*$, which are uniformly distributed in phase; here, the two sets of isochrons intersect transversally. Compared to Fig. 14(c), the periodic orbit Γ_s is more circular and the forward-time isochrons are better distributed around Γ_s. Figure 16(b) shows forward-time isochrons for Γ_s with arclength $L = 1.2$ and ten backward-time isochrons of $\mathbf{x}^*$ with the same phases as in panel (a). Here, the distribution of isochrons

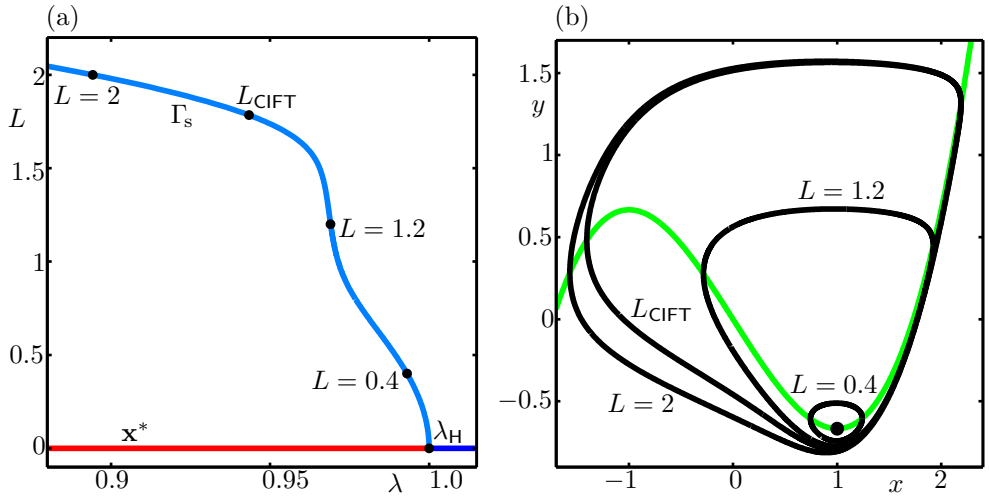

Figure 15: Canard explosion of the Van der Pol system (11) with $\varepsilon = 0.2$. Panel (a) shows a one-parameter bifurcation diagram in the (λ, L)-plane, where L the is arclength of the solutions. Shown is the equilibrium $\mathbf{x}^*$, (stable when blue, unstable when red) and the family of attracting periodic orbit Γ_s that emanates from a Hopf bifurcation at $\lambda_{\mathsf{H}} = 1$. The four labelled points correspond to cases when the periodic orbit Γ_s has arclength $L = 0.4$, $L = 1.2$, $L \approx 1.7842$ and $L = 2$, which are shown in panel (b), together with the critical manifold (green), and the equilibrium $\mathbf{x}^* = (1, -\frac{2}{3})$ at $\lambda = \lambda_{\mathsf{H}}$ (black dot).

around Γ_s is less uniform due to the slow-fast dynamics, but the sets of forward-time and backward-time isochrons still intersect transversally. Panel (c1) shows ten forward-time isochrons at $\lambda \approx 0.9434$, which is the approximate moment of the CIFT bifurcation. Also shown are thirteen backward-time isochrons of $\mathbf{x}^*$ that make cubic tangencies with the forward-time isochrons, as well as the trajectory O^* that passes through each of the cubic tangencies. Panel (c2) shows an enlargement of a region near the equilibrium $\mathbf{x}^*$, which shows several instances of cubic tangencies between the forward-time and backward-time isochrons along O^*. Panel (d1) shows ten forward-time isochrons for the periodic orbit Γ_s with arclength $L = 2$ and twelve corresponding pairs of backward-time isochrons of $\mathbf{x}^*$ that make quadratic tangencies with these forward-time isochrons. Also shown are the trajectories O^+ and O^-, which pass through each of the quadratic tangencies. Panel (d2) is an enlargement of a region near $\mathbf{x}^*$, which shows how the forward-time isochrons bend in order to make quadratic tangencies with the more radial backward-time isochrons along both O^+ and O^-.

Figures 14–16 provide numerical evidence to support the conjecture in Section 4.4 that a relaxation oscillation with a large time-scale separation exhibits non-transverse isochron intersections. On the other hand, close to the Hopf bifurcation, we expect the isochron intersections to be transverse. At a generic Hopf bifurcation a periodic orbit Γ_s is created with the same period as the natural period $T_{\mathbf{x}^*}$ of the equilibrium $\mathbf{x}^*$. All the forward-time isochrons are transverse to Γ_s and accumulate on $\mathbf{x}^*$, and all the backward-time isochrons are radial at $\mathbf{x}^*$ and accumulate on Γ_s. Hence, near a generic Hopf bifurcation, the foliations must be transverse. These arguments lead to the natural conjecture that for a sufficiently large time-scale separation, that is, for sufficiently small ε, a canard explosion is a general mechanism for creating a CIFT bifurcation.

6 Discussion

We addressed the question of how isochrons may change when parameters are varied, for example, in the well-known planar FitzHugh-Nagumo system that was already studied by Winfree. More specifically, we considered not only the usual (forward-time) isochrons of an attracting periodic orbit, but also introduced backward-time isochrons of a repelling periodic orbit or repelling equilibrium with complex-conjugate eigenvalues. The key

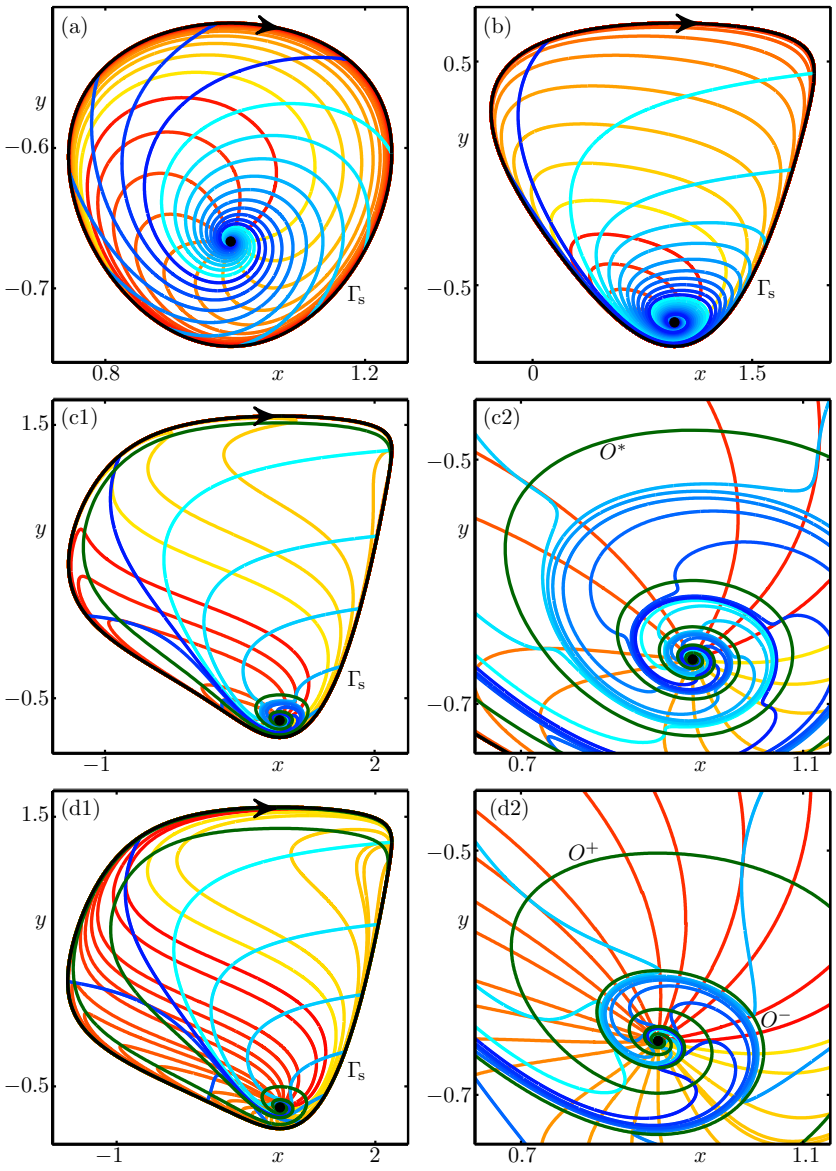

Figure 16: The CIFT bifurcation for (11) with $\varepsilon = 0.2$. Panels (a), (b), (c1) and (d1) show Γ_s at the four points labelled in Fig. 15 at different stages of the canard explosion. Each panel shows ten forward-time isochrons of Γ_s uniformly distributed in phase. Panels (a) and (b) show ten backward-time isochrons of $\mathbf{x}^*$ uniformly distributed in phase, which only intersect the forward-time isochrons transversally. Panel (c1) is approximately at the moment of the CIFT bifurcation where thirteen backward time isochrons of $\mathbf{x}^*$ make cubic tangencies with the shown forward-time isochrons; the trajectory O^* passes through all the cubic tangencies. Panel (d1) is after the CIFT bifurcation, showing twelve pairs of backward-time isochrons that make quadratic tangencies with the forward-time isochrons; the trajectories O^+ and O^- pass through each of the tangencies. Panels (c2) and (d2) show enlargements of panels (c1) and (d1), respectively, in a region near $\mathbf{x}^*$.

observation is that, in an annulus where they coexist, the two foliations by forward-time and by backward-time isochrons may generically either be transverse to each other or have quadratic tangencies. The transition happens at what we call a cubic isochron foliation tangency or CIFT bifurcation, which is a bifurcation of

codimension one. In fact, the quadratic tangencies of isochrons that are created must necessarily occur along two trajectories O^+ and O^-. Furthermore, the CIFT bifurcation is a regular, quadratic fold where these two trajectories of quadratic tangencies come together in a trajectory O^* of cubic tangencies and then disappear.

By computing isochrons with a boundary-value problem setup, we showed that a CIFT bifurcation indeed occurs in the FitzHugh-Nagumo system, namely when the time-scale separation parameter is increased. This led to the natural realization that a CIFT bifurcation can be generated by a sufficiently strong difference in time scales. To verify this observation we created two simple planar normal-form-type model vector fields with a parameter that introduces a time-scale separation in the phase plane. In the first model the time-scale separation acts globally between the two variables, while in the second model we rescale time in a small domain. Starting from two isochron foliations that intersect each other transversally, increasing the time-scale separation parameter indeed induces a CIFT bifurcation in both cases. Finally, we showed with the example of the Van der Pol system that a CIFT bifurcation also occurs naturally during a canard explosion, that is, in the transition from small periodic solutions created in a Hopf bifurcation to large relaxation oscillations.

Overall, the CIFT bifurcation emerges as a natural bifurcation in the context of multiple-time-scale systems. Roughly speaking, the foliations by forward-time and by backward-time isochrons are transverse when the time-scale separation is sufficiently small in the annulus where they coexist. When the time-sale separation is large, on the other hand, the two foliations must be expected to be non-transverse. Indeed, a first CIFT bifurcation can be identified as the transition mechanism. We remark that our local time-scale-perturbation model provides a generic example of two vector fields that are topologically (orbitally) equivalent in an annulus, but not conjugate, while having the same periodic orbits and periods.

When the respective time-scale parameter is increased further, the quadratic tangencies that have been created quickly develop into very sharp turns of (forward-time) isochrons that are associated with regions of strong phase sensitivity; see for example, [16, 23]. It is difficult to quantify this phase sensitivity by considering geometric properties (such as curvature) of the forward-time isochrons. Therefore, it is very helpful from a practical point of view that the well-defined and computable first CIFT bifurcation can be interpreted as the creation of phase sensitivity in the system. The price to pay, so to speak, is that one also needs to consider and compute backward-time isochrons.

We provided evidence for several general observations. Indeed, providing actual proofs remains an interesting challenge for future research. First of all, due to non-hyperbolicity it would require quite careful arguments to prove the continuity of isochrons through a Hopf bifurcation. A related question is to prove the transversality near a Hopf bifurcation of the isochron foliations between the bifurcating periodic orbit and equilibrium. It also seems possible to prove the non-transversality of the isochron foliations associated with a relaxation-oscillation of a planar system with a cubic nullcline; the idea would be to show that the singular case perturbs generically in such a way that forward-time and backward-time isochrons must have tangencies. These results would also imply the occurrence of a first CIFT bifurcation during a canard explosion.

Another interesting and challenging direction is to consider isochrons of system of dimension at least three. Indeed, our definitions are not restricted to the planar case and the CIFT bifurcation must also be expected to occur in higher dimensions. However, the topology and geometry of the isochrons may be much more complicated. Already in three dimensions the leaves of the forward-time and backward-time isochron foliations are surfaces. An important difference is also that, because periodic orbits do not form boundaries in this case, the region of existence of both types of isochrons is not necessarily a bounded domain of phase space. In fact, boundaries of basins may involve stable and unstable manifolds of saddle objects, including saddle equilibria and saddle periodic orbits. The characterization of isochron foliations in dimension three is a topic of our ongoing research. In particular, this work will require the development and implementation of algorithms for computing forward-time and backward-time isochrons as two-dimensional manifolds of the time-T_Γ map of a periodic orbit or equilibrium with a pair of complex-conjugate eigenvalues.

Acknowledgments

We thank John Guckenheimer, Yulij Ilyashenko, Jan Sieber and Freddy Dumortier for stimulating discussions on different aspects of isochrons.

This appendix provides detail about the bump function $g(x, y; \kappa)$ introduced in Section 5.2. We consider a symmetric polynomial $P(z)$ on the interval $z \in [-1, 1]$ such that

$$P(\pm 1) = 0, \quad P'(\pm 1) = 0, \quad P''(\pm 1) = 0, \quad \text{and} \quad P'''(\pm 1) = 0.$$

Furthermore, we require at the midpoint

$$P(0) = 1, \quad P'(0) = 0, \quad \text{and} \quad P''(0) = 0.$$

These eleven conditions are satisfied by a symmetric polynomial of degree twelve, namely,

$$P(z) = 1 - 9z^4 + 16z^6 - 9z^8 + z^{12}.$$

We evaluate $P(z)$ for $z = \frac{r-0.75}{0.025}$, where $r = \sqrt{x^2 + y^2}$ is the radial variable in the interval $[0.725, 0.775]$, and for $z = \frac{24\psi}{\pi}$, where $\psi = \arctan\left(\frac{y}{x}\right)$ is the angular variable in the interval $[-\frac{\pi}{24}, \frac{\pi}{24}]$. The bump function $g(x, y; \kappa)$ is now defined as

$$g(x, y; \kappa) = \begin{cases} 1 + \kappa P\left(\frac{r-0.75}{0.025}\right) P\left(\frac{24\psi}{\pi}\right), & \text{if } r \in [0.725, 0.775] \text{ and } \psi \in [-\frac{\pi}{24}, \frac{\pi}{24}], \\ 1, & \text{otherwise.} \end{cases}$$

References

[1] H. W. Broer, F. Dumortier, S. Van Strien, and F. Takens, *Structures in dynamics: finite dimensional deterministic studies*, vol. 2 of Studies in Mathematical Physics, Elsevier Science Publishers B.V., 1991.

[2] O. Castejón, A. Guillamon, and G. Huguet, *Phase-amplitude response functions for transient-state stimuli*, Journal of Mathematical Neuroscience, 3 (2013). 13.

[3] C. Chicone and W. Liu, *Asymptotic phase revisited*, Journal of Differential Equations, 204 (2004), pp. 227–246.

[4] M. Desroches, J. Guckenheimer, B. Krauskopf, C. Kuehn, H. M. Osinga, and M. Wechselberger, *Mixed-mode oscillations with multiple time scales*, SIAM Review, 54 (2012), pp. 211–288.

[5] M. Diener, *The canard unchained or how fast/slow dynamical systems bifurcate*, The Mathematical Intelligencer, 6 (1984), pp. 38–49.

[6] E. J. Doedel and B. E. Oldeman, *Auto-07P: Continuation and bifurcation software for ordinary differential equations*, with major contributions from Champneys, A. R., Dercole, F., Fairgrieve, T. F., Kuznetsov, Yu. A., Paffenroth, R. C., Sandstede, B., Wang, X. J., and Zhang, C.; available via http://cmvl.cs.concordia.ca/auto/ (2007).

[7] F. Dumortier, *Asymptotic phase and invariant foliations near periodic orbits*, Proceedings of the American Mathematical Society, 134 (2006), pp. 2989–2996.

[8] N. Fenichel, *Asymptotic stability with rate conditions for dynamical systems*, Bulletin of the American Mathematical Society, 80 (1974), pp. 346–349.

[9] R. FitzHugh, *Impulses and physiological states in theoretical models of nerve membrane*, Biophysical Journal, 1 (1961), pp. 445–466.

[10] J. Guckenheimer, *Isochrons and phaseless sets*, Journal of Mathematical Biology, 1 (1975), pp. 259–273.

[11] A. Guillamon and G. Huguet, *A computational and geometric approach to phase resetting curves and surfaces*, SIAM Journal on Applied Dynamical Systems, 8 (2009), pp. 1005–1042.

[12] M. W. Hirsch, C. C. Pugh, and M. Shub, *Invariant manifolds*, Bulletin of the American Mathematical Society, 76 (1970), pp. 1015–1019.

[13] G. Huguet and R. de la Llave, *Computation of limit cycles and their isochrons: Fast algorithms and their convergence*, SIAM Journal on Applied Dynamical Systems, 12 (2013), pp. 1763–1802.

[14] B. Krauskopf and T. Riess, *A Lin's method approach to finding and continuing heteroclinic connections involving periodic orbits*, Nonlinearity, 21 (2008), pp. 1655–1690.

[15] Y. A. Kuznetsov, *Elements of applied bifurcation theory 2nd Ed.*, vol. 112, Springer, 1998.

[16] P. Langfield, B. Krauskopf, and H. M. Osinga, *Solving Winfree's puzzle: the isochrons in the FitzHugh-Nagumo model*, Chaos, 24 (2014), p. 013131.

[17] A. Mauroy and I. Mezić, *On the use of Fourier averages to compute the global isochrons of (quasi) periodic dynamics*, Chaos, 22 (2012), p. 033112.

[18] A. Mauroy and I. Mezic, *Extreme phase sensitivity in systems with fractal isochrons*, arXiv:1408.2363, (2014).

[19] A. Mauroy, B. Rhoads, J. Moehlis, and I. Mezić, *Global isochrons and phase sensitivity of bursting neurons*, SIAM Journal on Applied Dynamical Systems, 13 (2014), pp. 306–338.

[20] J. Moehlis, *Improving the precision of noisy oscillators*, Physica D, 272 (2014), pp. 8–17.

[21] A. Nabi, M. Mirzadeh, F. Gibou, and J. Moehlis, *Minimum energy desynchronizing control for coupled neurons*, Journal of Computational Neuroscience, 34 (2013), pp. 259–271.

[22] H. Nakao, T. Yanagita, and Y. Kawamura, *Phase-reduction approach to synchronization of spatiotemporal rhythms in reaction-diffusion systems*, Physical Review X, 4 (2014), p. 021032.

[23] H. M. Osinga and J. Moehlis, *Continuation-based computation of global isochrons*, SIAM Journal on Applied Dynamical Systems, 9 (2010), pp. 1201–1228.

[24] M. Sabatini, *Non-periodic isochronous oscillations in plane differential systems*, Annali di Matematica Pura ed Applicata, 182 (2003), pp. 487–501.

[25] ——, *Linearizations, normalizations and isochrones of planar differential systems*, Rendiconti dell'Istituto di Matematica dell'Universit di Trieste, (2012), pp. 153–171.

[26] W. E. Sherwood and J. Guckenheimer, *Dissecting the phase response of a model bursting neuron*, SIAM Journal on Applied Dynamical Systems, 9 (2010), pp. 659–703.

[27] B. Van der Pol, *On relaxation oscillations*, The London, Edinburgh, and Dublin Philosophical Magazine and Journal of Science, 2 (1926), pp. 978–992.

[28] A. T. Winfree, *Patterns of phase compromise in biological cycles*, Journal of Mathematical Biology, 1 (1974), pp. 73–93.

[29] ——, *The Geometry of Biological Time, 2nd ed.*, vol. 12 of Interdisciplinary Applied Mathematics, Springer-Verlag, New York, 2001.